University of Alabama in Huntsville
LOUIS

Theses

UAH Electronic Theses and Dissertations

2012

Decomposition of radar amplitude tracks in the presence of multipath

Michael Anthony Johnson

Follow this and additional works at: https://louis.uah.edu/uah-theses

Recommended Citation

Johnson, Michael Anthony, "Decomposition of radar amplitude tracks in the presence of multipath" (2012). *Theses*. 555.
https://louis.uah.edu/uah-theses/555

This Thesis is brought to you for free and open access by the UAH Electronic Theses and Dissertations at LOUIS. It has been accepted for inclusion in Theses by an authorized administrator of LOUIS.

DECOMPOSITION OF RADAR AMPLITUDE TRACKS IN THE PRESENCE OF MULTIPATH

by

MICHAEL ANTHONY JOHNSON

A THESIS

Submitted in partial fulfillment of the requirements
for the degree of Master of Science in Engineering
in
The Department of Electrical and Computer Engineering
to
The School of Graduate Studies
of
The University of Alabama in Huntsville

HUNTSVILLE, ALABAMA

2012

In presenting this thesis in partial fulfillment of the requirements for a master's degree from The University of Alabama in Huntsville, I agree that the Library of this University shall make it freely available for inspection. I further agree that permission for extensive copying for scholarly purposes may be granted by my advisor or, in his/her absence, by the Chair of the Department or the Dean of the School of Graduate Studies. It is also understood that due recognition shall be given to me and to The University of Alabama in Huntsville in any scholarly use which may be made of any material in this thesis.

Michael Anthony Johnson

12/13/2011
(date)

THESIS APPROVAL FORM

Submitted by Michael Anthony Johnson in partial fulfillment of the requirements for the degree of Master of Science in Engineering in Electrical Engineering and accepted on behalf of the Faculty of the School of Graduate Studies by the thesis committee.

We, the undersigned members of the Graduate Faculty of The University of Alabama in Huntsville, certify that we have advised and/or supervised the candidate of the work described in this thesis. We further certify that we have reviewed the thesis manuscript and approve it in partial fulfillment of the requirements for the degree of Master of Science in Engineering in Electrical Engineering.

12/13/2011
Dr. Reza R. Adhami (Date) Committee Chair

Dec 14, 2011
Dr. Nagendra Singh (Date)

12/15/2011
Dr. Daniel Lawrence (Date)

2/10/11
Dr. Robert Lindquist (Date) Department Chair

12/19/11
Dr. Shankar Mahalingam (Date) College Dean

1/19/12
Dr. Rhonda Gaede (Date) Interim Graduate Dean

ABSTRACT

School of Graduate Studies
The University of Alabama in Huntsville

Degree Masters of Science in Engineering College/Dept. Engineering/Electrical and Computer Engineering

Name of Candidate Michael Anthony Johnson

Title Decomposition of Radar Amplitude Tracks in the Presence of Multipath

This thesis details the decomposition of the amplitude track of a low-angle target to allow independent analysis of target radar cross section (RCS), multipath, and target roll dynamics. This analysis is applicable to range radar that tracks surface-to-surface targets. Through the method developed in this thesis, rough surface parameters may be obtained by analysis of the amplitude track. Simulated radar tracks are analyzed using Fourier techniques and Empirical Mode Decomposition (EMD). Finally, a method of successive fitting and subtraction called A Priori Mode Decomposition (AMD) is developed. This method is similar to EMD but with a priori knowledge of the system. AMD was applied to the simulated environment in systematic fashion to a portion of parameter space showing robustness to changes in the modeled system parameters and noise.

Abstract Approval: Committee Chair
Dr. Reza R. Adhami

Department Chair
Dr. Robert Lindquist

Interim Graduate Dean
Dr. Rhonda Gaede

Contents

LIST OF FIGURES

FIGURE PAGE

LIST OF TABLES

TABLE PAGE

To my wife Jennifer, without her love and support none of this would have been possible.

CHAPTER 1

INTRODUCTION

We can lick gravity, but sometimes the paperwork is overwhelming.
- Wernher von Braun

1.1 Introduction

Since the birth of radar, the effects of multipath on low-angle targets has been a key features of radar signals. One of the earliest radar systems, the British HF Chain Home (CH) radar system, played a pivotal role in World War II and made use of the multipath lobes to determine the height of targets.[1] In this case, since the system was stationary, comparing the returns from receive antennas at multiple heights above ground allowed the variation in multipath nulls to be exploited. Since that time, radar systems for air targets have moved higher in frequency and primarily put narrow-angle beams on target. This has removed much of the effect of multipath and ground clutter. Modern radar that operates at microwave frequencies have short wavelengths and thus can experience dramatic multipath effects when used to track low-angle targets. This behavior affects both marine and ground radar.[2, 3] Though

used historically in the CH radar, in modern radar the multipath effects are considered an impairment.[4] Figure 1.1.1 shows the basic difference between high and low angle radars. This figure shows that the low-angle systems have the ground and multipath that arises from it in their antenna main beam and largest side lobes whereas these effects are greatly reduced in high-angle systems. Both high-angle and low-angle systems experience fluctuations in target RCS due to small changes in presented angle. This fluctuation is often treated statistically with Swerling models during the design phase of the radar [5] but is not often exploited during operation.

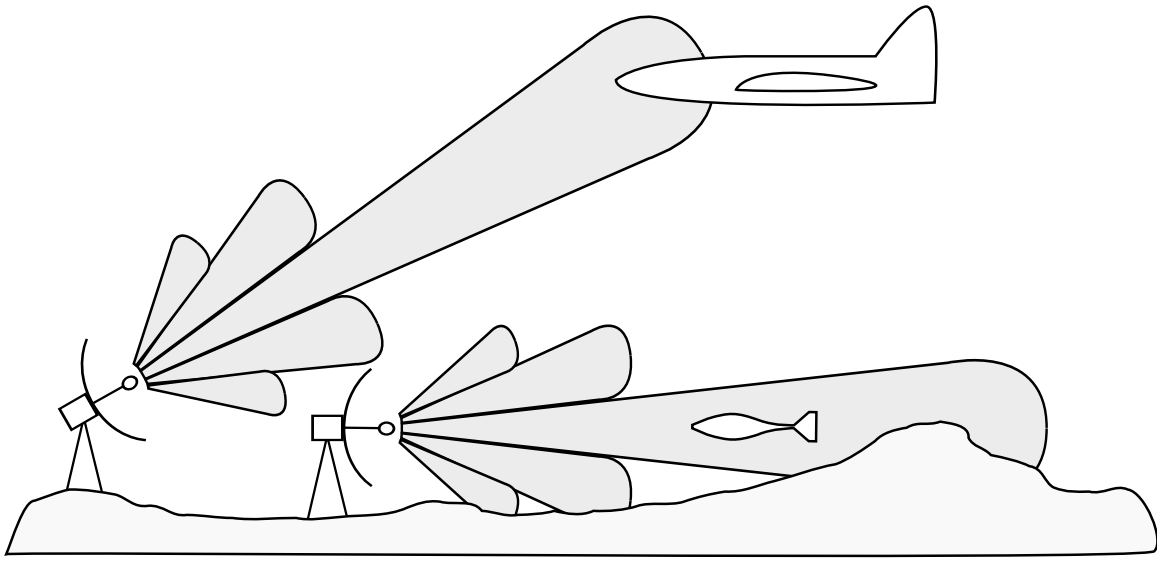

Figure 1.1.1: High-Angle Air Defense vs Low-Angle Ground or Marine Radar

1.2 Outline

This thesis details the decomposition of the amplitude track of a low-angle target to allow independent analysis of target radar cross section (RCS), multipath, and target roll dynamics. This analysis would be applicable to a range radar that tracks

surface to surface projectiles, rockets, and missiles. Typically amplitude data is not used beyond detection, but through the method developed in this thesis additional surface parameters may be obtained. In Chapter 2, an amplitude model of a target over a rough surface is developed for use in simulation of the return at low-angle. Radar tracks are then analyzed using Fourier techniques in Chapter 3. In Chapter 4, Empirical Mode Decomposition (EMD) is used to attempt to isolate the basic target return from the multipath and target fluctuation effects. In Chapter 5, a method of successive fitting and subtraction is developed similar to EMD but with a priori knowledge of the system. This method is then applied to tracks generated over a range of system parameters to determine the robustness of the method.

CHAPTER 2

RADAR SIGNAL MODEL

In theory, theory and practice are the same.
In practice they are different.
- Anonymous

2.1 Overview

We will consider the case shown in Figure 2.1.1 where a monostatic radar is located a distance R_z above the ground on the z-axis. The target to be tracked will fly a path parallel to the x-axis offset in the y dimension by T_y at an altitude of T_z above the ground. The terrain is approximated by the xy plane. The radar will be used for range r, and received power estimation P_{rx}.

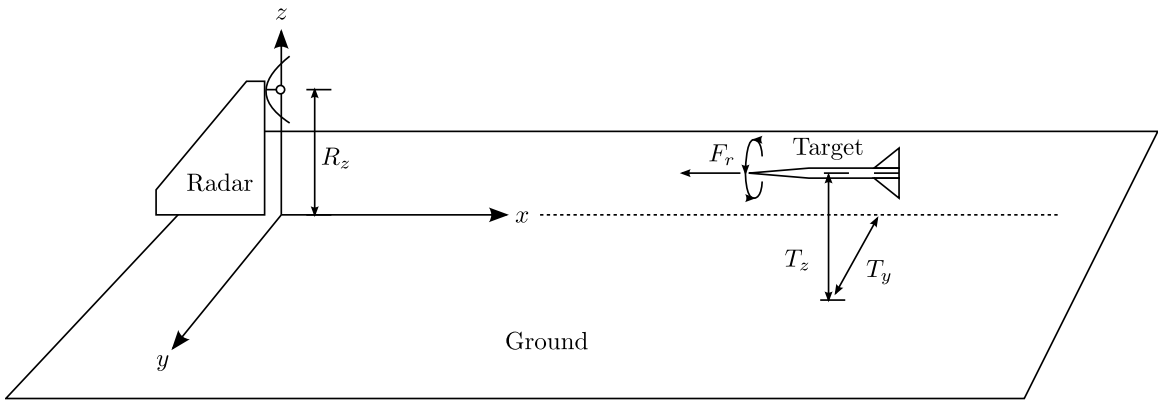

Figure 2.1.1: Coordinate System

The radar will operate on a signal with both an in-phase (I) and quadrature (Q) channel $z = I + jQ$. Target detection will be performed with a magnitude detector in the radar processor.

$$s = |z| = \sqrt{zz^*} = \sqrt{I^2 + Q^2} \tag{2.1.1}$$

The parameters considered for the baseline simulation are summarized in Table 2.1, 2.2, and 2.3.

Table 2.1: Radar Parameters

Parameter	Value
Radar Transmit Power	$P_t = 40.0\,dBm$
Antenna Gain	$G_r = 20.0\,dB$
Radar Frequency	$f_r = 40.0\,GHz$
Detection Bandwidth	$B = 3.0\,kHz$
System Noise Figure	$F = 10.0\,dB$
Radar Altitude	$R_z = 3.0\,m$

Table 2.2: Target Parameters

Parameter	Value
Target Cross Section	$\sigma_{rcs} = -15.0\,dBsm$
Target Altitude	$T_z = 2.0\,m$
Target Cross Range	$T_y = 1.0\,m$
Target Roll Rate	$F_s = 0.10\,{}^{1}/_{m}$
RCS Flutter	$A_r = 0.2\,dB$

Table 2.3: Terrain Parameters

Parameter	Value
Conductivity	$\mho = 1.0 \times 10^{-3}\,{}^{\mho}/_{m}$
Relative Dielectric Constant	$\epsilon = 10$
RMS Surface Roughness	$\sigma_h = 40.00\,mm$
Foliage Attenuation	$\alpha = 0.24\,Np/m$

2.2 Radar Range Equation

If we consider the target to be a non-fluctuating target, then the return is not a random variable and will be considered simply to be the received power P_s as calculated by the radar range equation.[6]

$$P_s = \frac{P_t G_r^2 \lambda^2 \sigma_{rcs}}{(4\pi)^3 r^4} \tag{2.2.1}$$

Using this equation and the values from Tables 2.1 and 2.2, we can generate the simulated received power vs range plot shown in Figure 2.2.1.

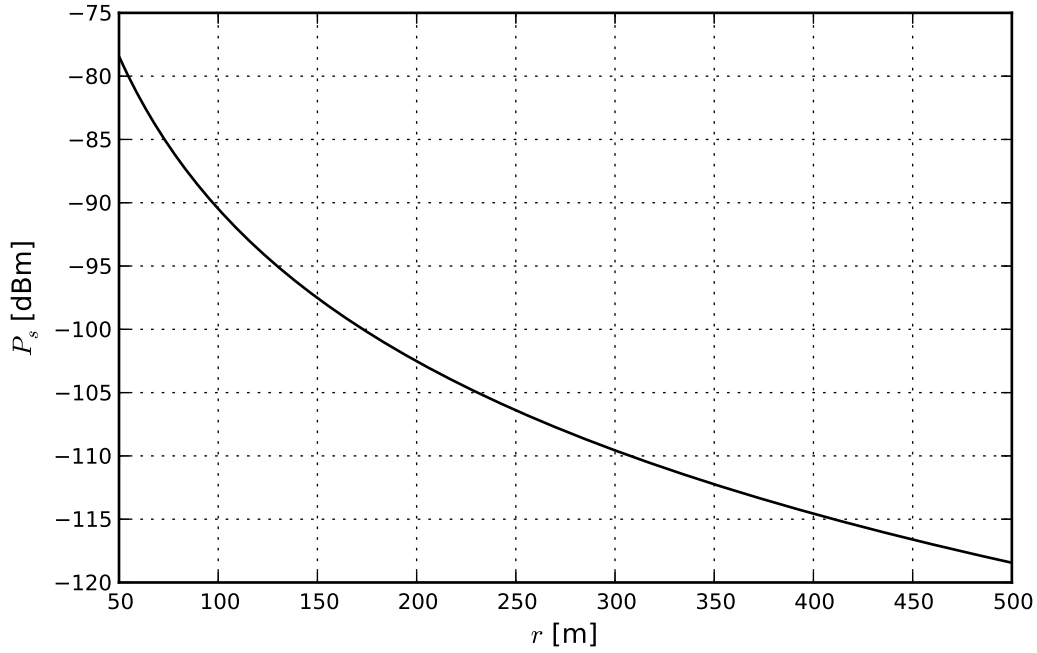

Figure 2.2.1: Target Return Power vs Range

2.3 Multipath

When the target is either low or distant, the amount of multipath effect may be significant. If we consider specular multipath only, the four primary signal paths we will consider are shown in Figure 2.3.1.

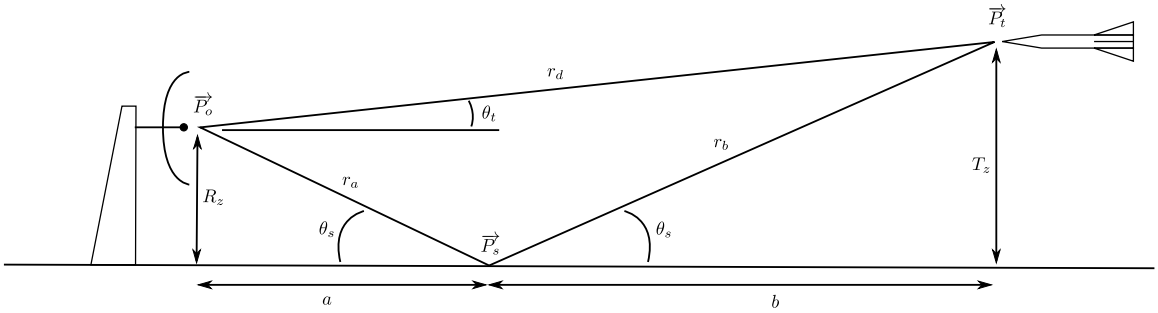

Figure 2.3.1: Multipath Paths

The path length r_d is the slant range from the radar to target.

$$r_d = \left|\overrightarrow{P_t} - \overrightarrow{P_o}\right| = \sqrt{(a+b)^2 + (T_z - R_z)^2} \tag{2.3.1}$$

The length of the indirect path through the specular point are easily solved in the plane that contains $\overrightarrow{P_o}$, $\overrightarrow{P_s}$, and $\overrightarrow{P_t}$.

$$a = \sqrt{\frac{r^2 - (R_z - T_z)^2}{\left(1 + \frac{T_z}{R_z}\right)^2}} \tag{2.3.2}$$

$$b = a\left(\frac{T_z}{R_z}\right) \tag{2.3.3}$$

$$r_a = \sqrt{a^2 + R_z^2} \tag{2.3.4}$$

$$r_b = \sqrt{b^2 + T_z^2} \tag{2.3.5}$$

The grazing angle of the indirect path is also easily derived and is given below:

$$\theta_g = \arctan\left(\frac{R_z}{a}\right) = \arctan\left(\frac{T_z}{b}\right) \tag{2.3.6}$$

The azimuthal angle to the target from the radar θ_c is given below:

$$\theta_c = \arcsin\left(\frac{P_{t\,x} - P_{r\,x}}{a+b}\right) \tag{2.3.7}$$

The direct path is simply twice the Euclidean distance between $\overrightarrow{P_o}$ and $\overrightarrow{P_t}$. The specular point $\overrightarrow{P_s}$ is the point at which the grazing angle θ_s from the radar to the point is equal to the grazing angle from the target to the same point. It is given by Equation 2.3.8.

$$\overrightarrow{P_s} = (P_{r\,x} + a\cos(\theta_c))\,\hat{x} + (P_{r\,y} + a\sin(\theta_c))\,\hat{y} + 0\hat{z} \tag{2.3.8}$$

The four paths we will consider are:

1. Direct path $l_d = 2r_d$
2. Indirect path through the specular point outgoing $l_a = r_a + r_b + r_d$
3. Indirect path from the target back to the radar $l_b = r_d + r_b + r_a = l_a$
4. Indirect path both directions $l_c = r_a + r_b + r_b + r_a$

For a trajectory over a perfect electrical conductor (PEC), we would expect the received signal to receive interference from each path equally resulting in the received signal modulated by a propagation factor:

$$F_p = e^{jl_d 2\pi/\lambda} + 2e^{jl_a 2\pi/\lambda} + e^{jl_c 2\pi/\lambda} \tag{2.3.9}$$

This has a "chirp" characteristic as a function of range as shown in Figure 2.3.2. From this plot we can see that the signal can destructively cancel and also constructively add, since the signal can be increased by up to four times the propagation factor is as much as $12dB$.

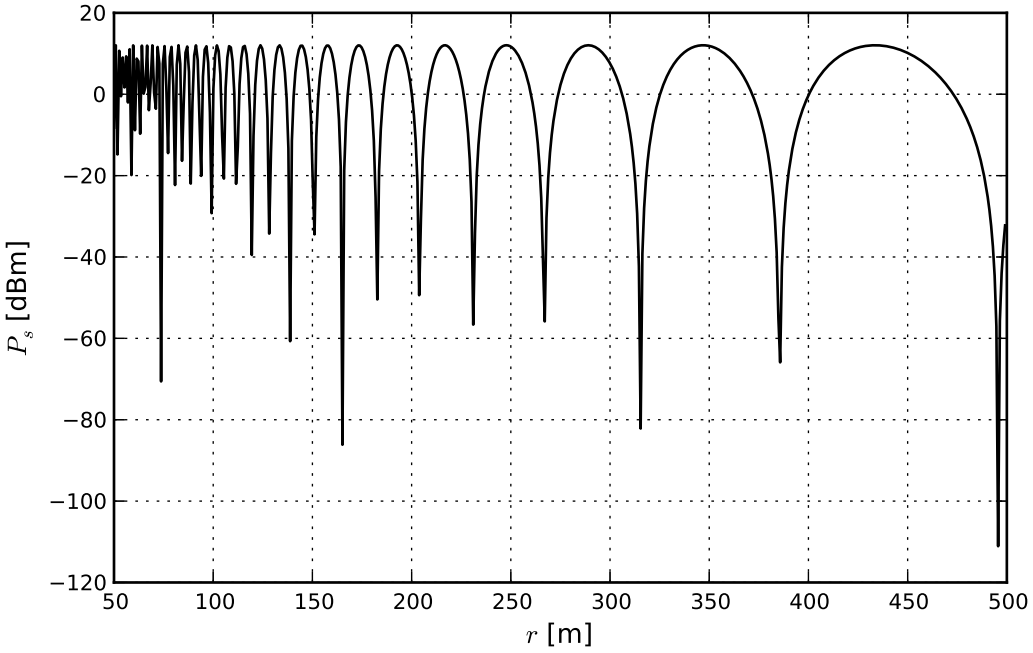

Figure 2.3.2: Propagation Factor Over a PEC

We are unlikely to encounter data taken over a perfect conductor. Initially we will consider a perfectly smooth, perfectly flat dielectric slab and consider its reflection coefficient similar to the development in [7]. The terrain will be assumed to have a relative dielectric constant

$$\epsilon_{rc} = \frac{\epsilon}{\epsilon_o} - 60i\lambda\sigma \tag{2.3.10}$$

where we will initially assume the nominal value of $\epsilon = 10\,\epsilon_o$ and $\sigma = 1.0 \times 10^{-3}\,\text{℧}/m$. Additionally, the permeability shall be assumed to be $\mu_{rc} = 1$ and the normalized admittance:

$$Y = \sqrt{\frac{\epsilon_{rc}}{\mu_{rc}}} \tag{2.3.11}$$

The reflection coefficients for the vertical polarization R_o^{vv} and horizontal polarization R_o^{hh} are derived in [8][7] and given below:

$$R_o^{vv}(\theta_g) = \frac{Y^2 \sin\theta_g - \sqrt{Y^2 - \cos^2(\theta_g)}}{Y^2 \sin\theta_g + \sqrt{Y^2 - \cos^2(\theta_g)}} \tag{2.3.12}$$

$$R_o^{hh}(\theta_g) = \frac{\sin\theta_g - \sqrt{Y^2 - \cos^2(\theta_g)}}{\sin\theta_g + \sqrt{Y^2 - \cos^2(\theta_g)}} \tag{2.3.13}$$

For the given parameters, the phase of R_o^{VV} changes abruptly from 180^o to 0^o at $\theta_g = 17.5^o$, $\left|R_o^{VV}\right|$ and $\left|R_o^{hh}\right|$ vary over angle according Figure 2.3.3.

A target flying over this smooth terrain is not affected much (less than 3dB) by the terrain at the small grazing angles ($\theta_g < 3^o$) that we see over most of the flight path. We can see this if we modify Equation 2.3.9 to include the effects of reflection coefficient

$$F_p = e^{jl_d 2\pi/\lambda} + 2R_o(\theta_g)\, e^{jl_a 2\pi/\lambda} + R_o^2(\theta_g)\, e^{jl_c 2\pi/\lambda} \tag{2.3.14}$$

which results in roll-off seen in Figure 2.3.4

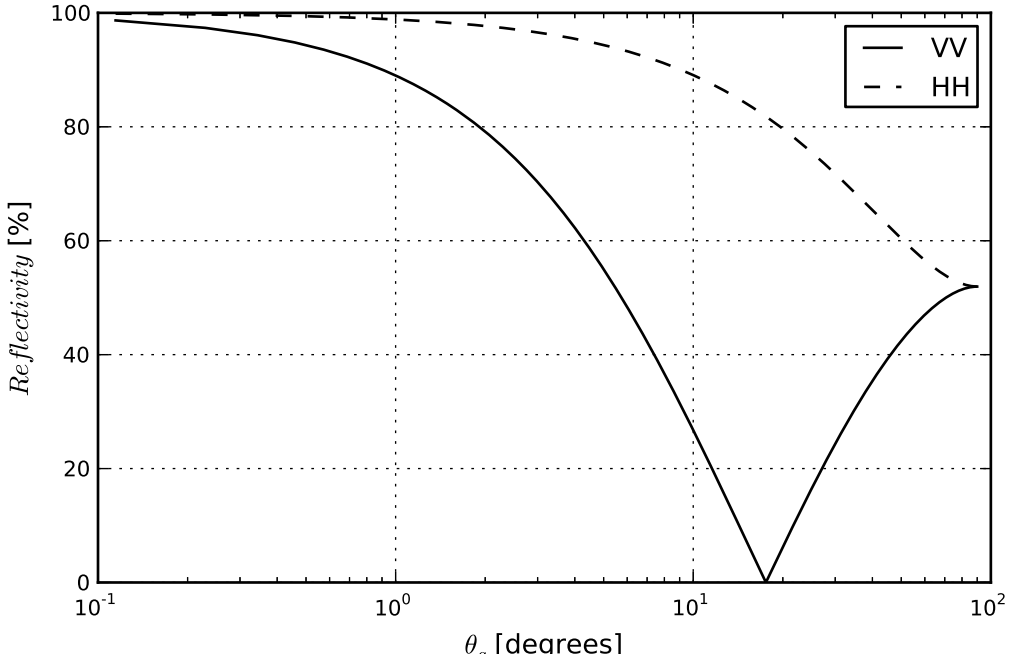

Figure 2.3.3: Variation of $\left|R_o^{VV}\right|$and $\left|R_o^{HH}\right|$ vs θ_g

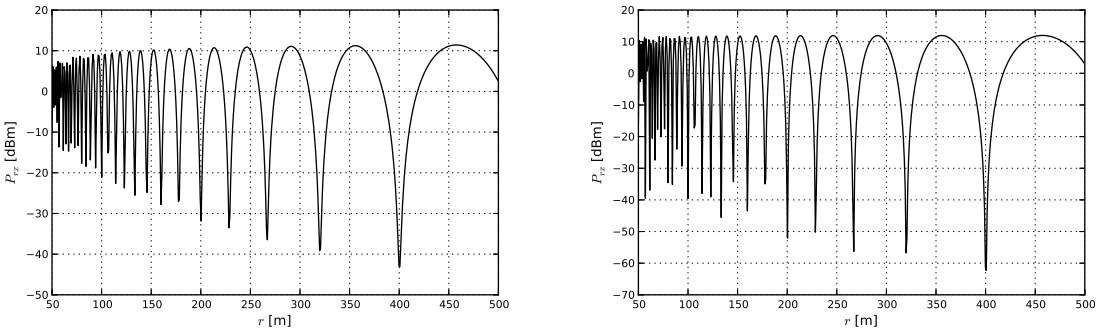

(a) $\left|R_o^{VV}\right|$ (b) $\left|R_o^{HH}\right|$

Figure 2.3.4: Propagation Factor Over Smooth Ground

No terrain is perfectly flat, so we must modify the reflection coefficient due the the effect of uneven rough terrain. For terrain with a Gaussian distribution of terrain

height where the rms roughness $\sigma_h = 40.00\,mm$ we can use the following relation derived in [7] and given below:

$$R_s = \rho_s R_o \tag{2.3.15}$$

where

$$\left\langle |\rho_s|^2 \right\rangle = e^{-\left(\frac{4\pi\sigma_h \sin\theta_g}{\lambda}\right)^2} \tag{2.3.16}$$

plotting $\sqrt{\left\langle |\rho_s|^2 \right\rangle}$ as a function of angle in Figure 2.3.5 we can see that the reflection coefficient rapidly approaches zero for even small angles at our wavelength. If we apply this to Equation 2.3.14 once again we get

$$F_p = e^{jl_d 2\pi/\lambda} + 2R_{\rho o}\left(\theta_g\right)\rho_s\left(\theta_g\right)e^{jl_a 2\pi/\lambda} + R_o^2\left(\theta_g\right)\rho_s^2\left(\theta_g\right)e^{jl_c 2\pi/\lambda} \tag{2.3.17}$$

This roll off has the effect shown in Figure 2.3.6.

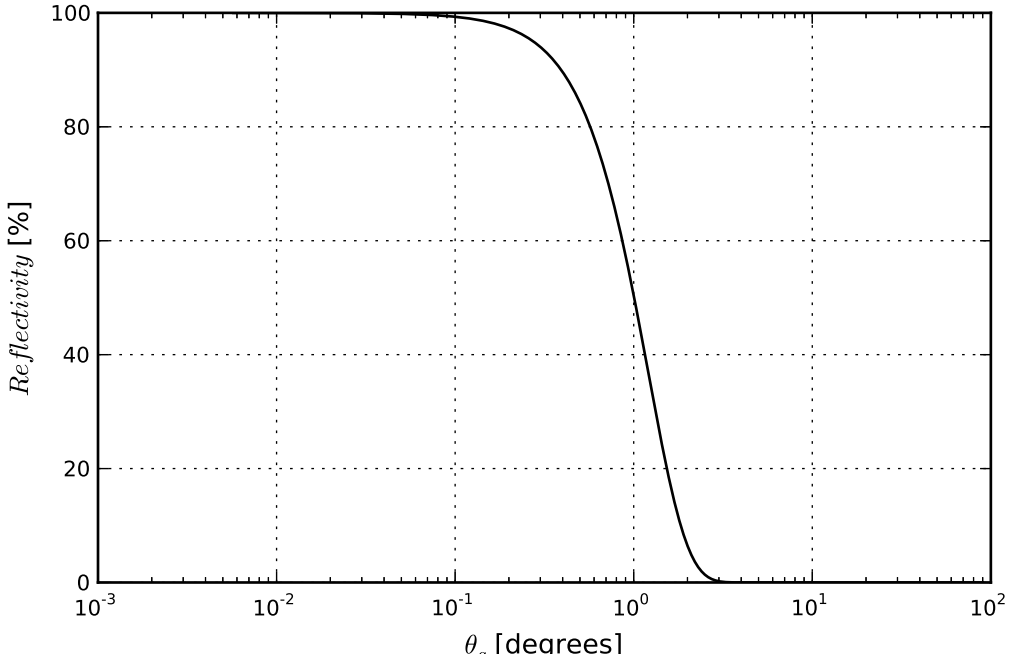

Figure 2.3.5: $\sqrt{\left\langle |\rho_s|^2 \right\rangle}$

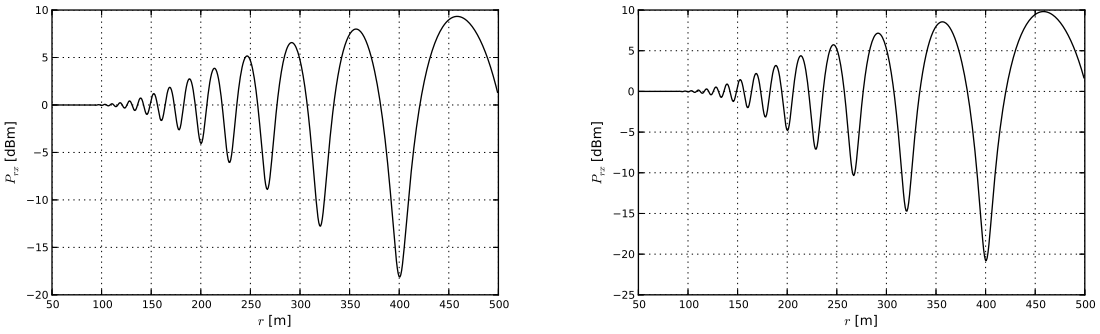

(a) $\left|R_o^{VV}\right|$ (b) $\left|R_o^{HH}\right|$

Figure 2.3.6: Propagation Factor Over Rough Ground

Finally at extremely low grazing angles on rough foliage-covered surfaces such as grass, the incident and reflected rays must pass through a significant amount of

biomass. In this case, the path length traversed by the reflected ray is determined by the height of the ground cover which will be taken to be the same as the RMS surface roughness σ_h and is shown in Figure 2.3.7.

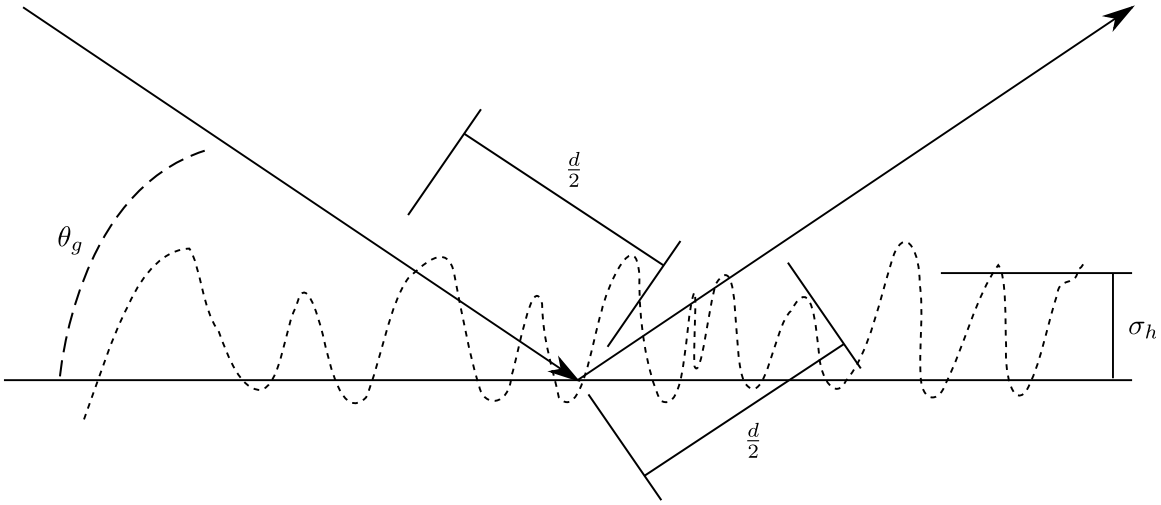

Figure 2.3.7: Attenuation Path

$$d = \frac{2\sigma_h}{\sin(\theta_g)} \tag{2.3.18}$$

This path length then results in a path attenuation of:

$$\langle A \rangle = e^{-2\alpha d} = e^{-4\alpha\sigma_h/\sin(\theta_g)} \tag{2.3.19}$$

where α is the path attenuation constant. We will use $\alpha = 0.24\,Np/m$ for the frequency of interest which results in the angle dependent falloff shown in Figure 2.3.8 for $\sigma_h = 40.00\,mm$.[9]

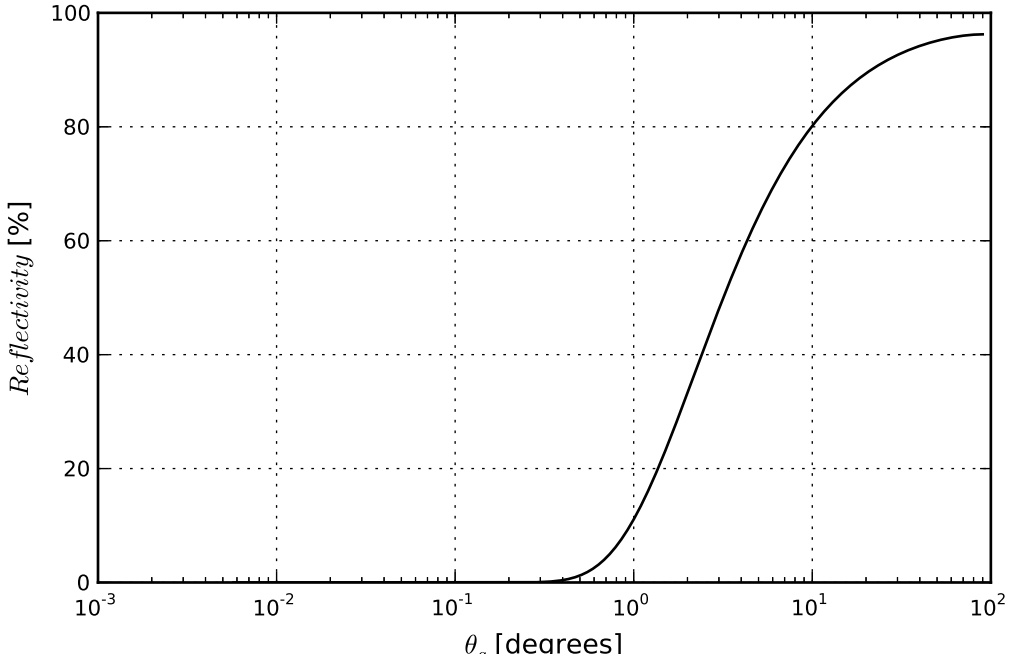

Figure 2.3.8: $\langle A \rangle$

If we apply this to Equation 2.3.9 once again we get

$$F_p = e^{jl_d 2\pi/\lambda} + 2R_{\rho o}\left(\theta_g\right)\rho_s\left(\theta_g\right)A\left(\theta_g\right)e^{jl_a 2\pi/\lambda} + R_o^2\left(\theta_g\right)\rho_s^2\left(\theta_g\right)A^2\left(\theta_g\right)e^{jl_c 2\pi/\lambda} \quad (2.3.20)$$

which results in a ripple seen in Figure 2.3.9. We can see in this figure that since the effect of surface roughness drives the reflection coefficient to zero at steep angles and the attenuation drives it to zero at extremely shallow angles. The difference we saw in Figure 2.3.4 between polarizations has been covered by the surface roughness effect.

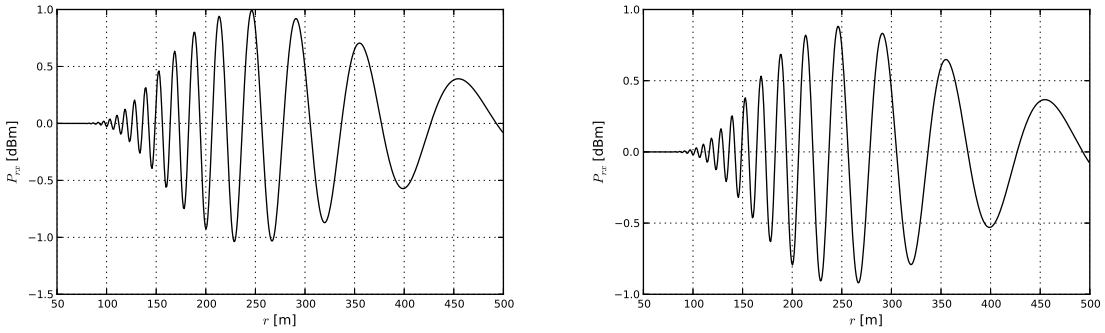

(a) $\left|R_o^{VV}\right|$ (b) $\left|R_o^{HH}\right|$

Figure 2.3.9: Propagation Factor Over Rough Ground with Foliage

Finally, if we assume vertical polarization and apply the rough surface propagation factor to the radar range equation, we get a simulated radar amplitude shown in Figure 2.3.10 containing the effects of multipath.

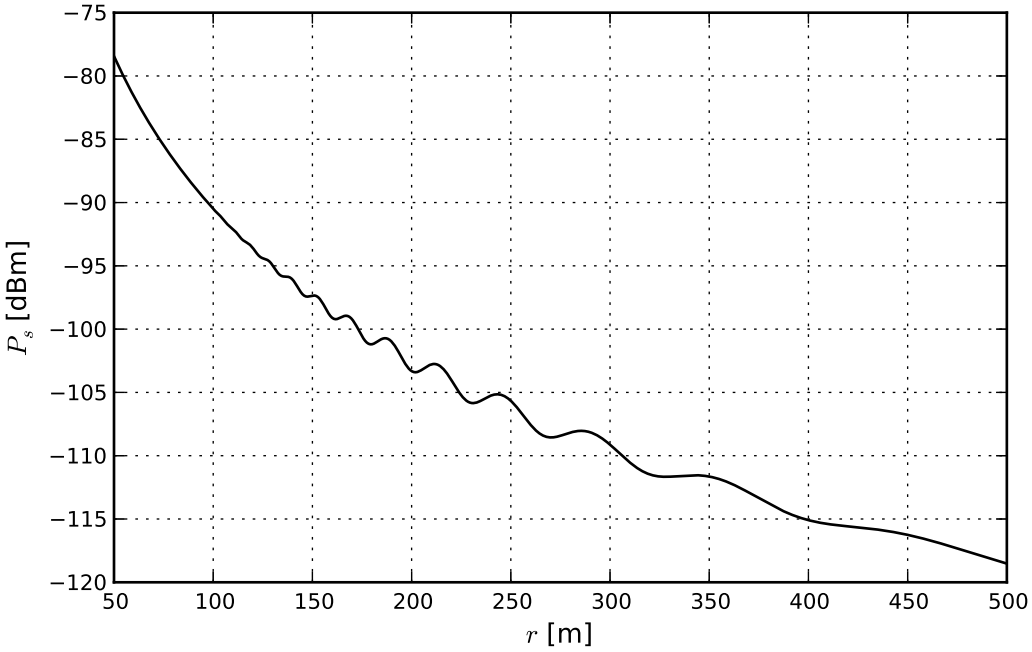

Figure 2.3.10: Received Power vs Range Over Rough Terrain

2.4 RCS Modulation

Projectiles are commonly spin-stabilized to enhance stability during flight. The presence of fins can make the RCS of the target vary as a function of roll angle.[10] If we assume the target is traveling parallel to the x-axis and it rolls once every R_d, the spatial frequency is $F_s = {}^1/_{R_d} = 0.10\,{}^1/_m$ and raises or lowers the RCS by $A_r = 0.2\,dB$. We can model this fluctuation with:

$$RCS_{roll}(x) = RCS_o + A_r \sin(2\pi x F_s + \phi) \tag{2.4.1}$$

If the target is spin-stabilized by fins once the roll rate achieves steady state, the spatial frequency of the RCS variation is primarily dependent on velocity. If we observe the target over a short distance the roll rate will be constant. It should be noted that R_d is the distance required to roll to a similar symmetric orientation, e.g., if the target has 4 fins it would roll through a cycle 4 times per actual revolution of the target. If we add the fluctuating cross section according to the parameters in Table 2.2, we get the result shown in Figure 2.5.2.

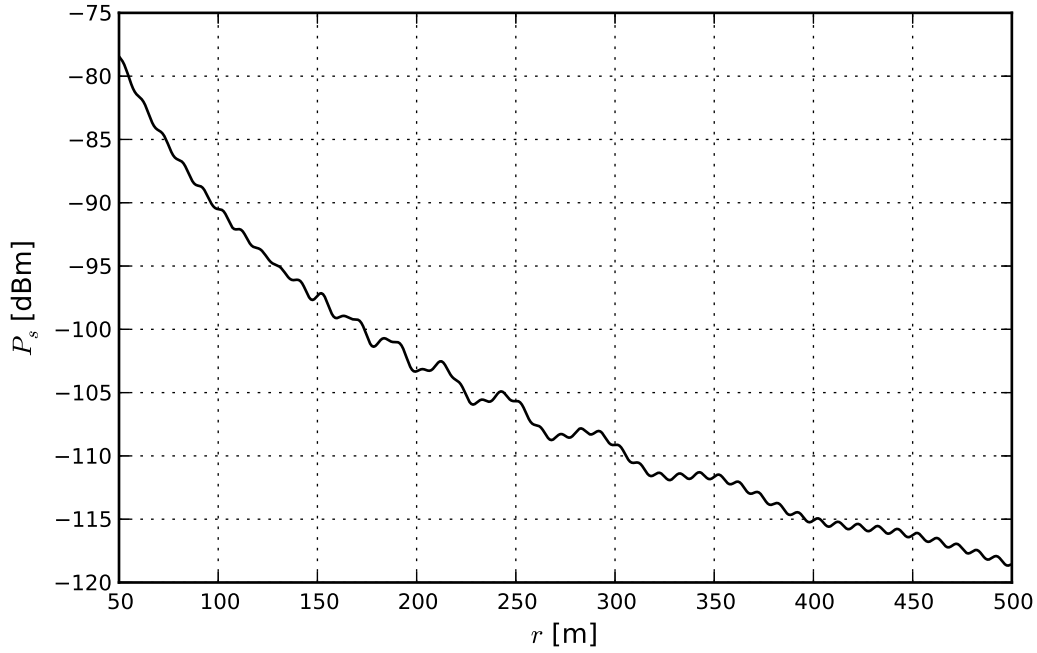

Figure 2.4.1: Rolling Target Over Rough Terrain

2.5 Noise

We will additionally assume that the I and Q channels have identical independently distributed [i.i.d.] white noise with power $\sigma_g^2/2$ in each for a total noise power of σ_g^2 in the signal z. The PDF of the noise at the output of the detector is then given by the Rayleigh distribution in Equation 2.5.1.[11]

$$p_r(r) = \begin{cases} \frac{2r}{\sigma_g^2} e^{-r^2/\sigma_g^2} & r \geq 0 \\ 0 & otherwise \end{cases} \tag{2.5.1}$$

The expected value of Equation 2.5.1 is given by

$$E[r] = \sigma_g \frac{\sqrt{\pi}}{2} = \mu_r \tag{2.5.2}$$

The receiver noise is represented by a random variable ν which will be generated in simulation by a complex signal with Gaussian random variables in the I and Q components.

$$\nu = \nu_I + j\nu_Q \tag{2.5.3}$$

Once we generate the noise signal we can use the relation

$$\sigma_g^2 = \frac{4}{\pi}\mu_\nu^2 \tag{2.5.4}$$

as a convenient way to validate our simulated noise by comparing the magnitude mean to the RMS power.

$$\sigma_g^2 = \frac{1}{N}\sum_{k=1}^{N} \nu_k \nu_k^* \tag{2.5.5}$$

The total noise power in ν is σ_g^2 which is given by

$$\sigma_g^2 = kTBF \tag{2.5.6}$$

where thermal noise density is $N_o = 10\log(kT) = -174.0\,dBm/Hz$, B is the detection bandwidth $B = 3.0\,kHz$, and F is the noise figure of the receiver $F = 10.0\,dB$.

$$\sigma_g^2 = -174.0\,dBm/Hz + 10\log(3.0\,kHz) + 40.0\,GHz = -129.2\,dBm \tag{2.5.7}$$

This allows us to model the received power at the detection of

$$P_{rx} = P_s + \nu \tag{2.5.8}$$

which is shown in Figure 2.5.1. This is the magnitude detector output for a point target flying the free space trajectory described by Section 2.1.

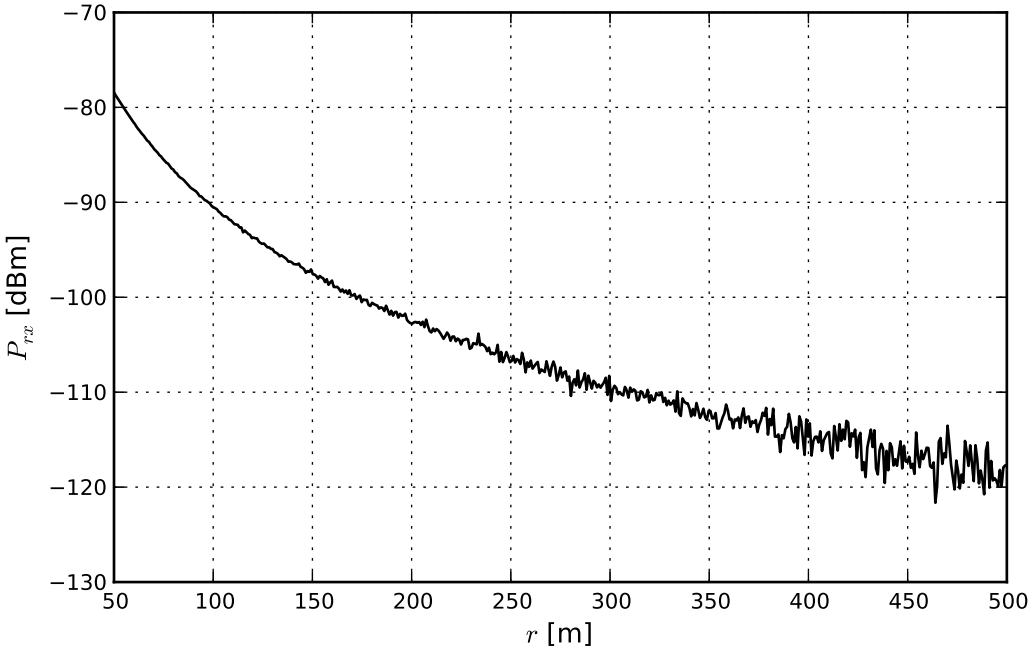

Figure 2.5.1: Received Power vs Range with Receiver Noise

Finally, we can show the received power of the signal corrupted by all sources including noise in Figure 2.5.2.

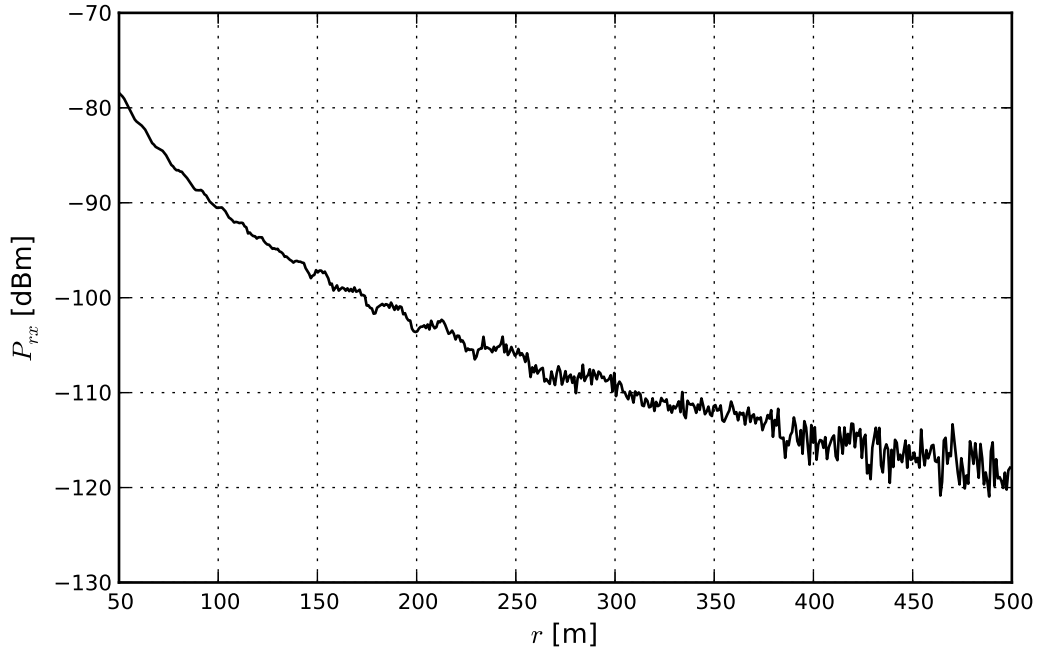

Figure 2.5.2: Fully Modeled Power Return

CHAPTER 3

FOURIER ANALYSIS

Sometimes when you connect the dots you get a picture.
Other times you just have a bunch of dots.
- RK

3.1 Introduction

Traditional data-analysis generally falls into two broad categories: decomposition into a series of basis functions or model-based approaches. In this thesis we are considering decomposition, of which the most common method by far is Fourier analysis. The data to be analyzed is sampled so the Discrete Fourier Transform (DFT) is used, this method attempts to decompose the data into a set of orthogonal basis functions consisting of sinusoids. Though this method is simple, it produces good results for many applications due to the abundance of systems in the natural world that obey a law similar to Equation 3.1.1.

$$\ddot{x} = -kx \tag{3.1.1}$$

This is Hook's Law which applies not only to the mass on a spring problem we studied in high school, but to most problems involving compression, bending, or torsion of

a material. In addition this same form shows itself in the acoustic wave equation, electromagnetic wave equation, and many others.

3.2 Discrete Fourier Transform (DFT)

In general a transform decomposes an input signal $x(t)$ into a series of coefficients c_n that represent the amplitude of each member of a set of basis functions $g_n(t)$ which when summed would result in the reconstruction of the original signal.

$$x(t) = c_0 g_0(t) + c_1 g_1(t) + c_2 g_2(t) + \ldots = \sum_{k=0}^{N} c_k g_k(t) \tag{3.2.1}$$

In the case of the Exponential Fourier Series, the basis functions are the complex exponentials $g_k(t) = e^{-jk\omega_0 t}$ at integer multiples of the frequency ω_0 which is related to the sampled interval T by the relation $\omega_0 = \frac{2\pi}{T}$. This choice of basis functions is useful since they have to form of solutions to 3.1.1. In addition, the criteria that they form is a set of orthogonal basis satisfying Equation 3.2.2:

$$\int_0^T g_k(t)\, g_{k'}^*(t)\, dt = \int_0^T e^{-jk\omega_0 t} e^{jk'\omega_0 t} dt = T\delta_{kk'} \tag{3.2.2}$$

where $\delta_{nn'}$ is the Kronecker delta function. When $k = k'$ Equation 3.2.2 is simply $\int_0^T dt = T$ and when $k \neq k'$ Equation 3.2.2 is of the form $\int_0^T e^{j\left(k'-k\right)\omega_0 t} dt$ which since k and k' are both integers means that we are integrating an oscillating function over an integer number of cycles which is zero. To determine the optimal value, in a minimum square error sense, of each coefficient c_k in the series we can use:

$$c_k = \frac{\int_0^T x(t)\, g_k(t)\, dt}{\int_0^T g_k(t)\, g_k^*(t)\, dt} = \frac{1}{T}\int_0^T x(t)\, e^{-jk\omega_0 t} dt \tag{3.2.3}$$

If we assume our input signal is sampled at intervals separated by Δt then $t = n\Delta t$ and $N = {}^{T}/_{\Delta t}$. This allows us to change Equation 3.2.3 to the discrete sum:

$$c_k = \frac{1}{N}\sum_{n=0}^{N-1} x(n)\, e^{-jk2\pi n/N} \tag{3.2.4}$$

Equation 3.2.4 forms the DFT, the $\frac{1}{N}$ normalization can be removed and we will use:

$$X(k) = \sum_{n=0}^{N-1} x(n)\, e^{-j2\pi nk/N} \tag{3.2.5}$$

For example the simple signal

$$x(t) = e^{j2\pi 2.0t} \tag{3.2.6}$$

and its DFT $X(f)$ are shown in figure 3.2.1. It can be seen that $x(t)$ in this case enjoys compact support in the frequency domain by the observing the sparseness of $X(f)$, in fact $X(f)$ has only one non-zero coefficient.

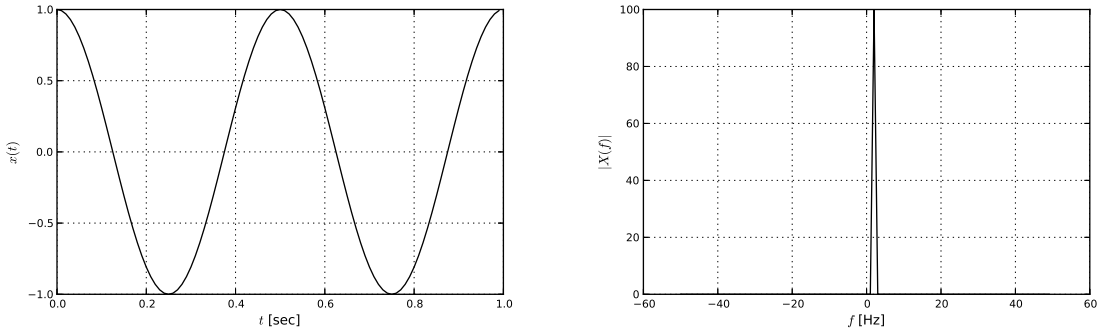

(a) $\mathrm{Re}\,(x\,(t))$ (b) $|X\,(t)|$

Figure 3.2.1: Complex Exponential with Integer Number of Cycles

If we look at the case of:

$$x\,(t) = e^{j2\pi 2.5t} \tag{3.2.7}$$

and its DFT $X\,(f)$ in Figure 3.2.2 this minor change has made $X\,(f)$ much less sparse; in fact all the coefficients in $X\,(t)$ are non-zero.

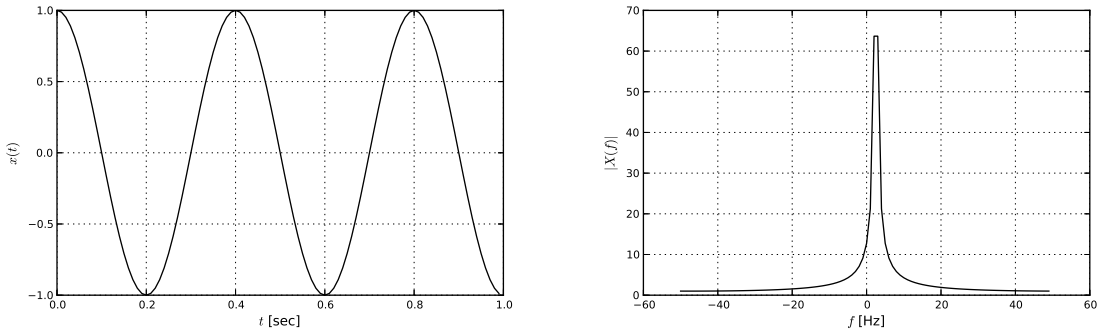

(a) $\mathrm{Re}\,(x\,(t))$ (b) $|X\,(t)|$

Figure 3.2.2: Complex Exponential with Fractional Number of Cycles

3.3 Limitations of the DFT

By necessity, Fourier techniques require the satisfaction of the Dirichlet condition, or periodic matching of the boundary conditions, to be valid. Sampled signals that do not fit an integer number of periods into the sample period as well as signals that are intermittent do not fit this criteria. Figure 3.3.1 illustrates this problem by showing what Equation 3.2.7 looks like when sampled for three seconds in Figure 3.3.1a and what it looks like when w·sampled for one second and repeated three times in Figure 3.3.1b. The difference is dramatic and obvious.

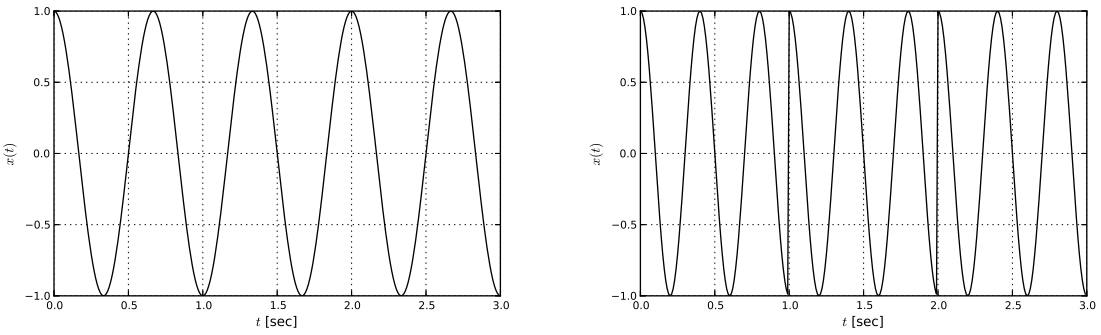

(a) Sampled for 3.0 Seconds

(b) Sampled for 1.0 Seconds and Repeated

Figure 3.3.1: Equation 3.2.7 Extended to 3.0 seconds Two Ways

The repeated case shown in Figure 3.3.1b is what the result of the DFT transform is based on whereas the desired result would likely be the transform of the time extended case in Figure 3.3.1a. This disconnect between the desire to estimate the actual power spectral density (PSD) of a signal and what is returned by the DFT is at the heart of the problem with the Fourier transform.

It is instructive to look at the origin of the "tails" in spectrum shown in Figure 3.2.2. The DFT can be considered a bank of filters with each their centers placed at $\omega_k = {}^{2\pi k}/_{N},\ k = 0 \ldots (N-1)$. The time-domain input is a simple rectangular pulse

$$x(n) = \begin{cases} x_i(n) & 0 \leq n \leq (N-1) \\ 0 & n > (N-1) \end{cases} \tag{3.3.1}$$

where $x_i(n)$ is the data input to the finite length DFT which results in the familiar sinc filter response of:

$$X(m,k) = \frac{N}{2} \frac{sin(\pi(k-m))}{\pi(k-m)} \tag{3.3.2}$$

This filter shape is shown in Figure 3.3.2 and annotated to highlight the fact that $X(m,k)$ has a zero response at each bin center except for k. In Figure 3.3.3 we show the overlapped response of the entire filter bank, on the left a signal is place between bins and we see that there is a response from each of the filters in the bank. On the right a signal is placed in the center of a bin and there is only response from the filter centered on that bin. This leads us to a common method of mitigating these "tails" or "leakage" by shaping the filter response to localize the signal energy more compactly in frequency.

The customary solution is to apply a time-domain weighting to the data set prior to the DFT to set the shape of the filters. These windowing functions generally approach zero at the beginning and end of the samples, so this can also be seen as artificially enforcing the Dirichlet condition. For example, the Hamming window can

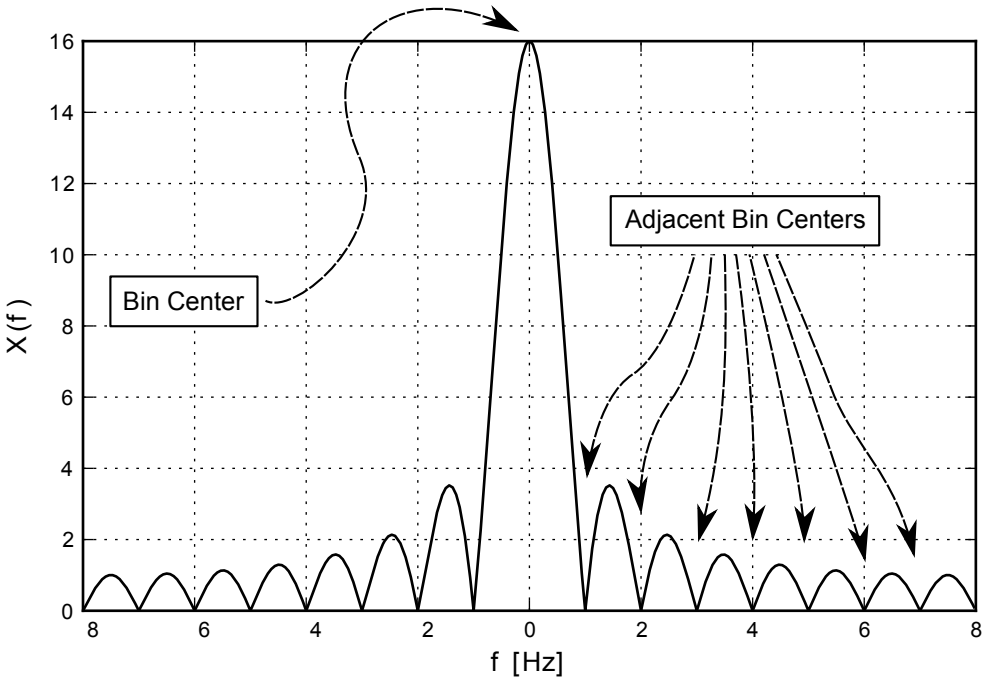

Figure 3.3.2: DFT Filter Shape

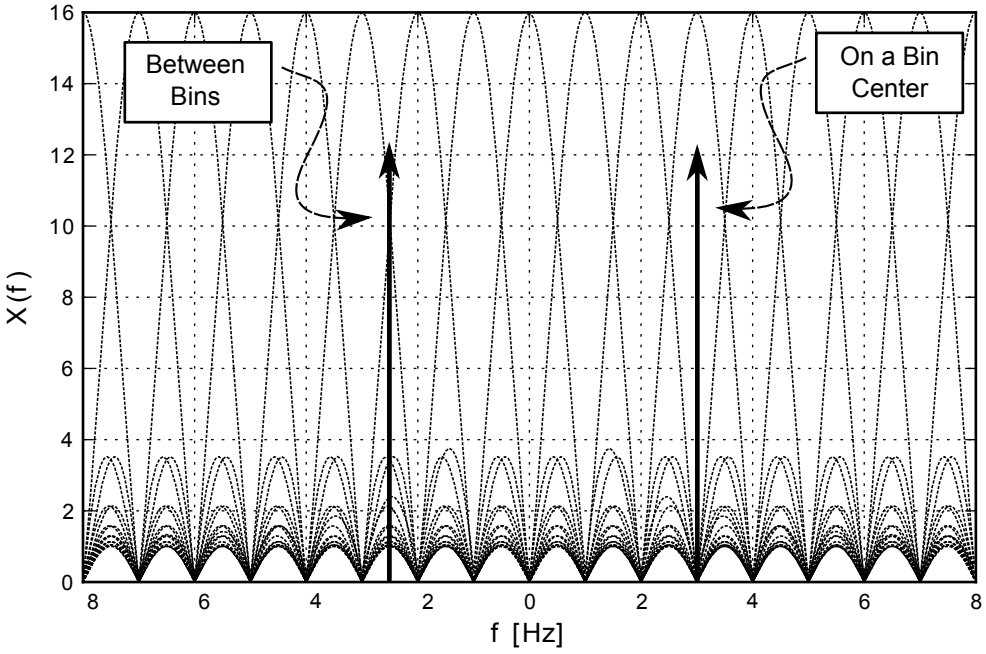

Figure 3.3.3: DFT Filter Bank

be defined[12] in the time domain as:

$$w(n) = 0.54 - 0.46\cos\left(\frac{2\pi n}{N-1}\right) \qquad 0 \leq n \leq N-1 \tag{3.3.3}$$

if we apply this weight to the signal described in Equation 3.2.7 we can see the result in Figure 3.3.4.

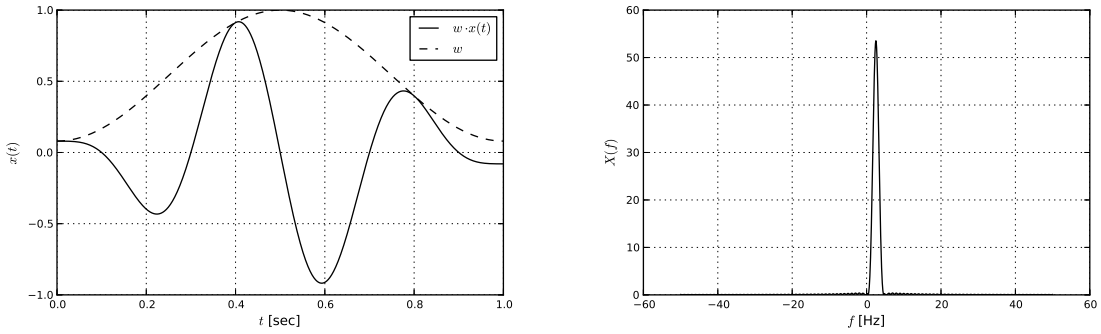

(a) Weighted Signal $x(t) = w(t)\,x_i(t)$ and Hamming Weight $w(t)$

(b) DFT of Weighted Signal $X(f)$

Figure 3.3.4: Hamming Window

If we compare plot the Hamming filter band in Figure 3.3.5 and then compare it to Figure 3.3.3, we can see that though we now have a small response in all the filter at bin center, we have reduced the response from all but the adjacent bins to tones mid-bin, thus improving the situation greatly.

Windowing has limits in that it cannot deal effectively with data sets that contain highly non-stationary signals.[12] To state this another way, Equation 3.2.5 uses a complex exponential with a constant frequency across the entire sampling interval as the basis function so a signal that contains an intermittent signal will not

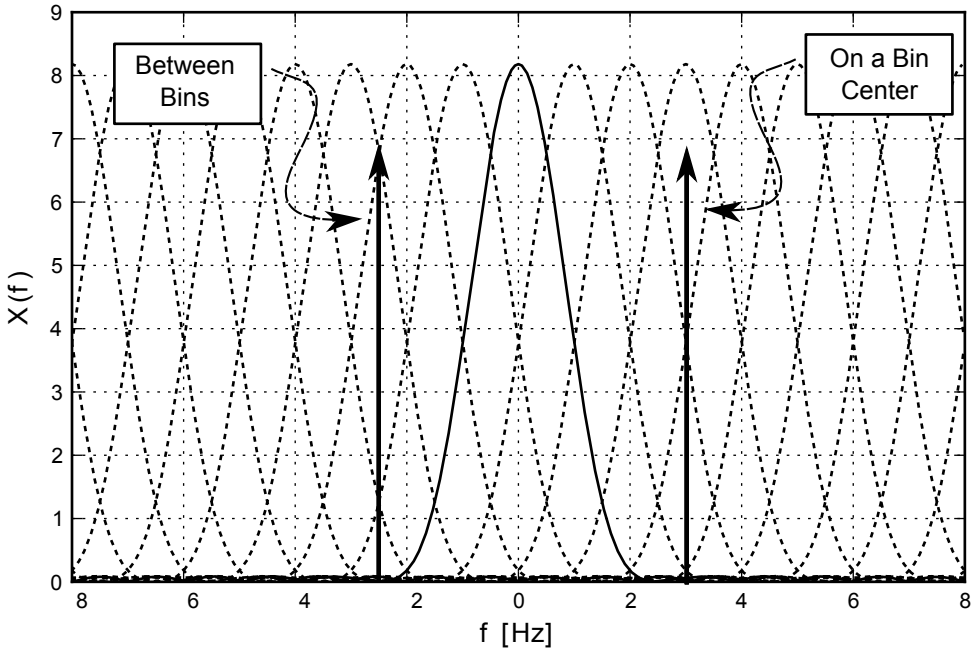

Figure 3.3.5: DFT Filter Bank

enjoy compact support. In addition, when windowing is used in the time domain to better localize the signal in the frequency domain, unequal weighting of non-stationary signal components will occur. For example if we consider the signal:

$$x(t) = \begin{cases} 2t + e^{j2\pi t4} + 0.002 \cdot e^{j2\pi t60} & t < 0.5 \\ 2t + e^{j2\pi t16} + 0.002 \cdot e^{j2\pi t60} & t \geq 0.5 \end{cases} \tag{3.3.4}$$

This signal is continuous in the time domain as can be seen in Figure 3.3.6. The DFT of the signal described by Equation 3.3.4 with the Hamming window applied is also shown in Figure 3.3.6 along with the DFT of $x(t) = \sqrt{2}e^{j2\pi t4} + \sqrt{2}e^{j2\pi t16} + 0.002 \cdot e^{j2\pi t60}$. The presence of the frequency discontinuity produces large tails that are not

mitigated by the Hamming window. The effect on the spectrum due to this kind of change is so dramatic that it completely hides the third smaller continuous tone. This is not surprising since the discontinuity occurs at the point that the window has the least effect.

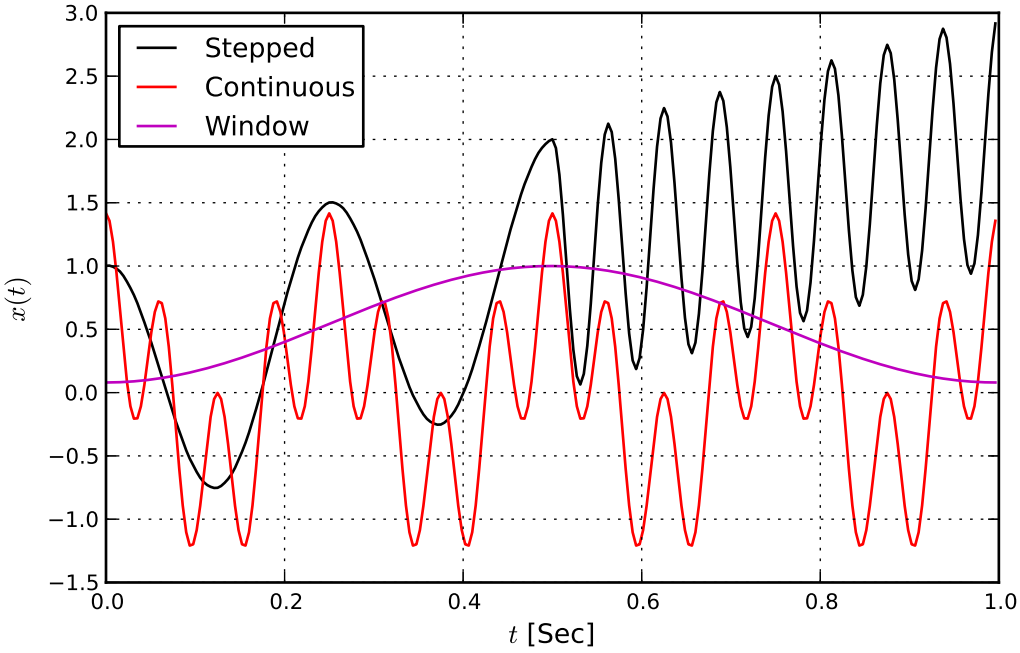

(a) Non stationary signal

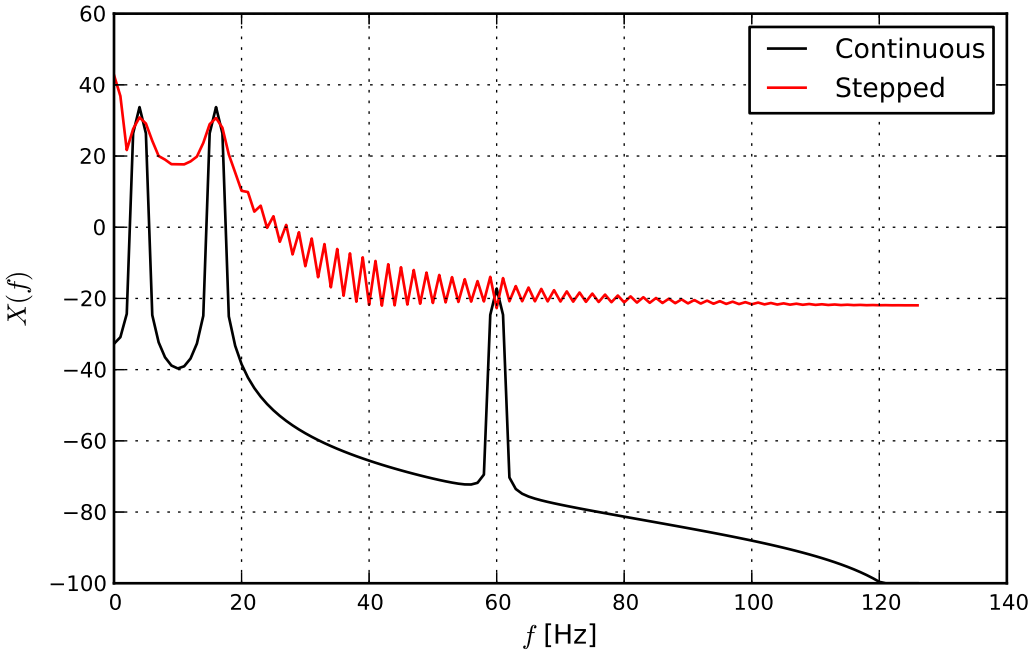

(b) DFT of Non Stationary Signal and Two Tones

Figure 3.3.6: Non Stationary Two Tone Example

3.4 Short Time FFT

A widely-used method for analysis of non-stationary signals is the Short-Time Fourier Transform (STFFT), also know as the spectrogram. The information of speech and music is encoded in the time-varying amplitude and frequency of the component parts, and analysis of these signals makes extensive use of the spectrogram. A STFFT is nothing more than the application of a window with limited-time extent that is shifted through the signal to form spectral estimates at different times in the signal. The result is then plotted as a function of time and frequency

$$w_t(\tau) = w(\tau - t) \tag{3.4.1}$$

where $w(t) \to 0$ on a time scale that is small compared to the total length of the input signal.

$$X_{ST}(k, m) = \sum_{n=0}^{N-1} w(n - m)\, x(n)\, e^{-j2\pi nk/N} \tag{3.4.2}$$

Algorithmically from the spectrogram, we simply split the input signal into a set of overlapping or contiguous sub-series that are each then transformed with a windowed FFT. If we apply the STFFT to the signal described by Equation 3.3.4, we could get any of a family of spectrograms such as the the ones shown in Figure 3.4.1. Both of the spectrograms are of the same input data and use a Hamming window, but the width of Figure 3.4.1b was made small, giving it good time localization and poor frequency localization. Figure 3.4.1a used a wide window, giving it good frequency resolution but poor time resolution. This is the basic trade-off that limits the ability

of the STFFT to localize a signal in time or frequency but not both.[13] When the spectrogram is formed with a short window in Figure 3.4.1b, there is not enough process gain to see the tone, but the time of the step is well-defined. When a long window is used in Figure 3.4.1a the tone is discernable, but the time around the step is corrupted by the step-event obscuring details close the time of the step.

3.5 FFT analysis of RADAR data

Using the target model developed and described in Chapter 2, we will attempt to analyze the target track using Fourier methods. Initially we will perform the DFT on the noise-free track shown in Figure 2.4.1 with and without Hamming weights applied. The result is shown in Figure 3.5.1. Since the track has a large $A_r = 0.2\,dB$ fluctuation at a spatial frequency of $F_s = 0.10\,{}^1\!/_m$, we can easily see a peak in the windowed FFT; it is however much less obvious in the rectangular FFT. When the FFT is applied to the signal from Figure 2.5.2, which includes noise, we see similar results, which are shown in Figure 3.5.2.

Finally, we form spectrograms with good frequency and time resolution in Figures 3.5.3a and 3.5.3b respectively. No features of this signal are made apparent by either type of spectrogram.

Having seen the ability of the windowed FFT to reveal the roll flutter peak, a simple peak interpolator was used to estimate the frequency and amplitude of the roll flutter using the FFT. The simulation was swept through parameter space by varying the RCS of the target from -35 to -10 dBsm and then adjusting the cross range of

the target T_y and target altitude T_z from 0 to 10 meters at the nominal RCS of $-15.0\,dBsm$. At each point in parameter space estimates of the roll parameters were made in Monte Carlo fashion by recording the median result of 10 noise realizations. The results of this are shown in Figure 3.5.4 and 3.5.5. It can be seen that the method estimates the roll frequency well when the RCS is bigger than -27dBsm. The estimate quality does not appear to be impacted by the altitude or cross-range position of the target as long at the RCS is large enough.

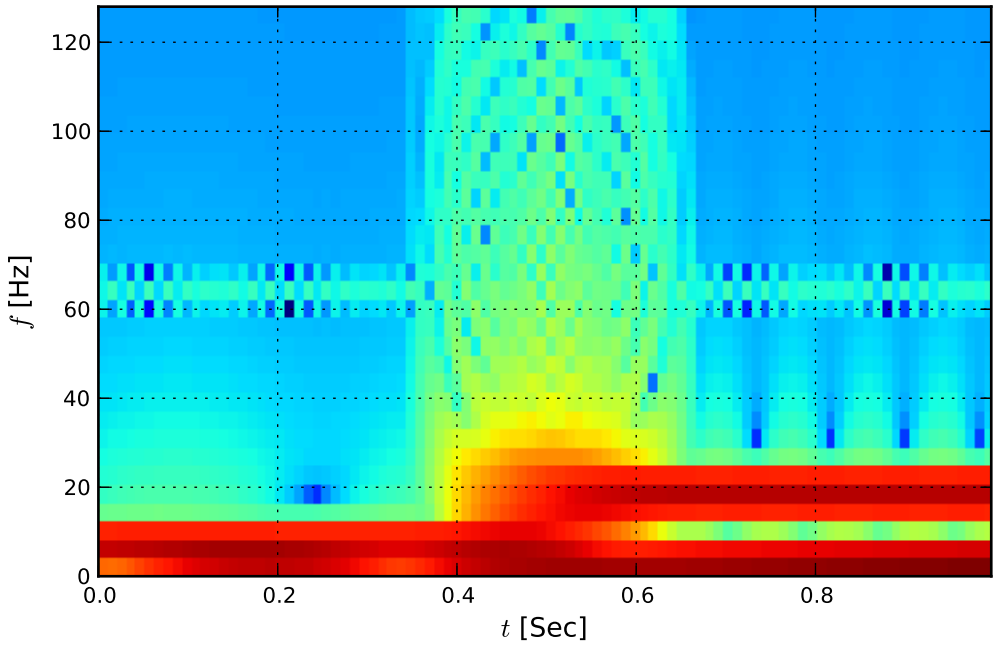

(a) Wide Window

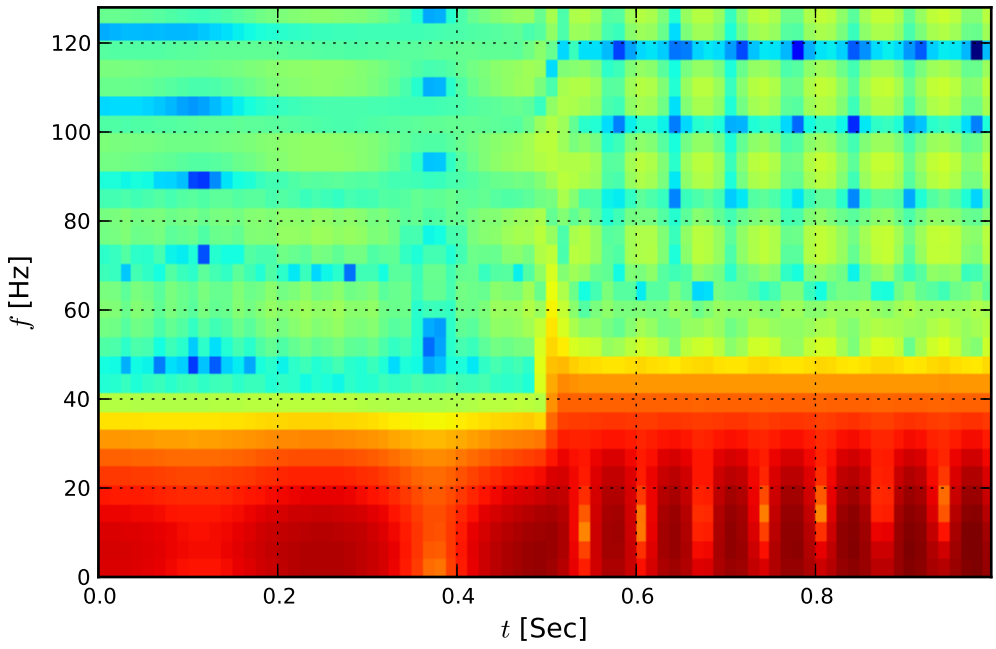

(b) Narrow Window

Figure 3.4.1: Short Time FFT (Spectrogram)

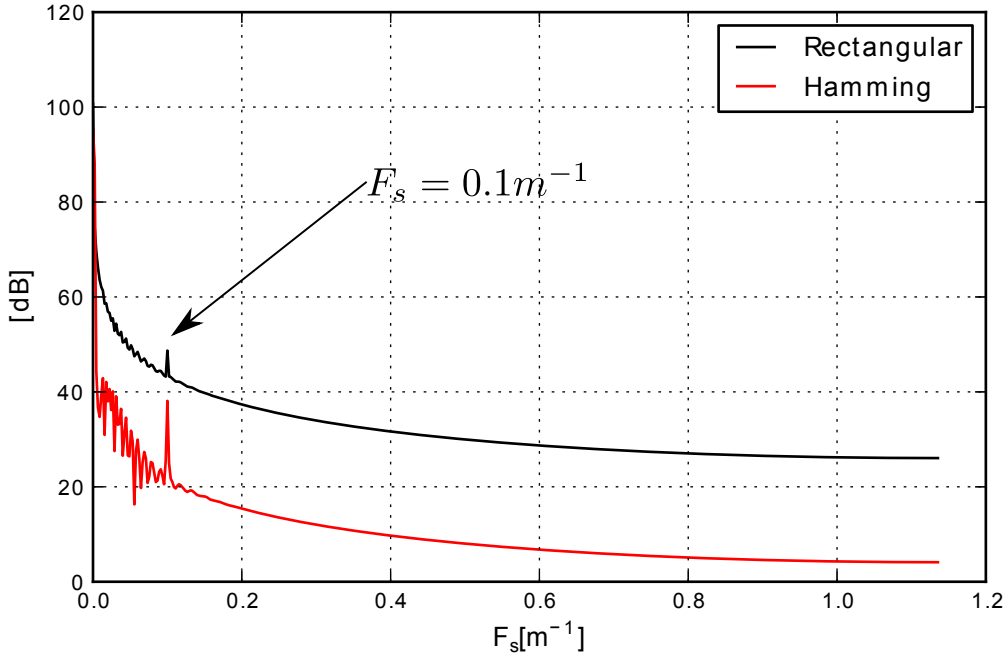

Figure 3.5.1: DFT of Noise-Free Target Track

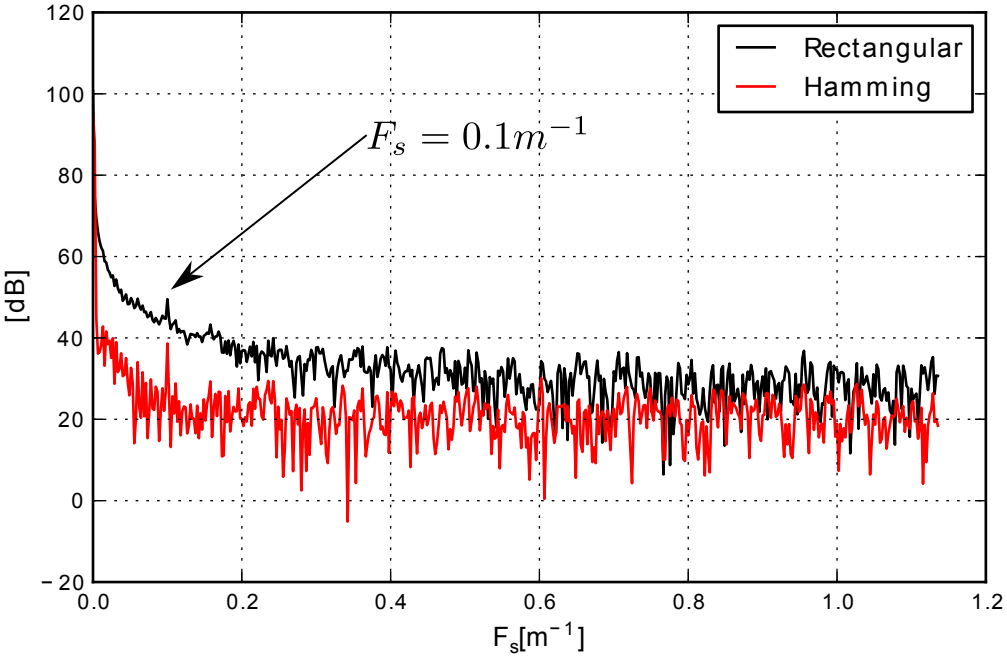

Figure 3.5.2: DFT of Target Track

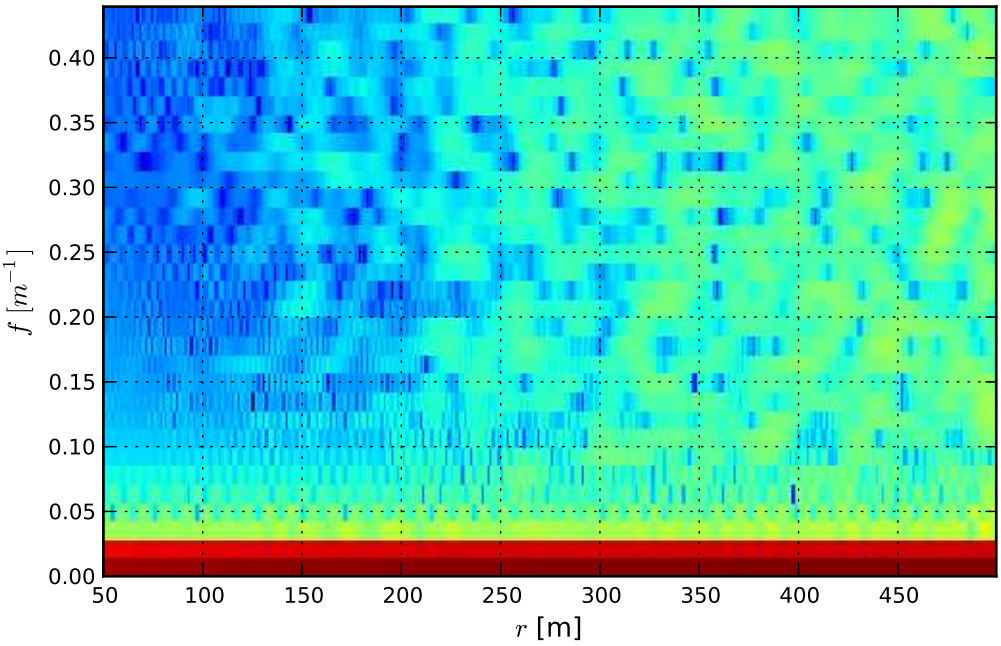

(a) Wide Window

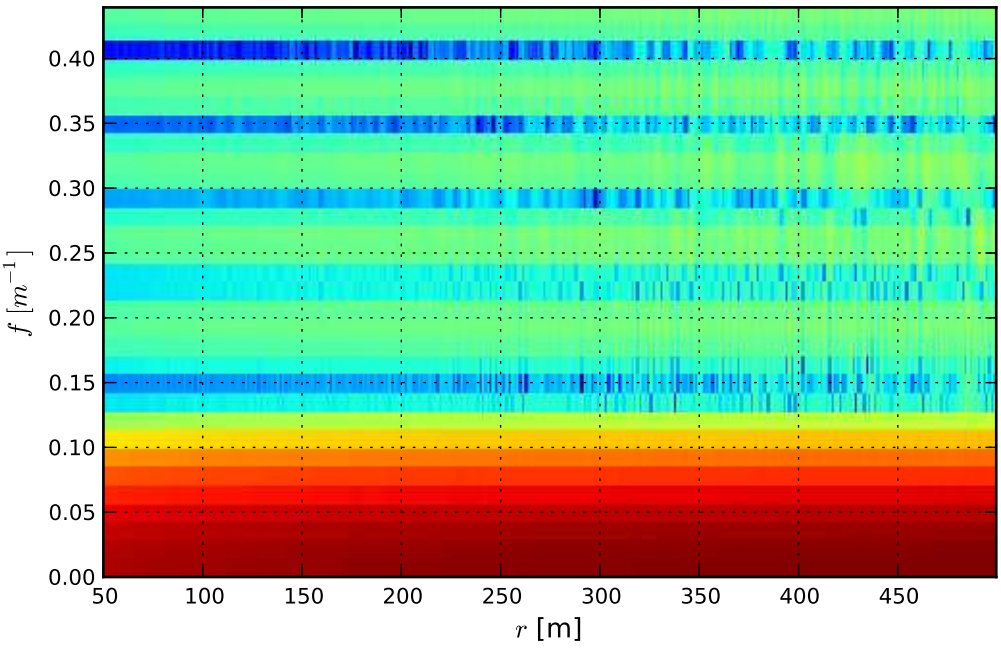

(b) Narrow Window

Figure 3.5.3: Short Time FFT (Spectrogram) of Target Track

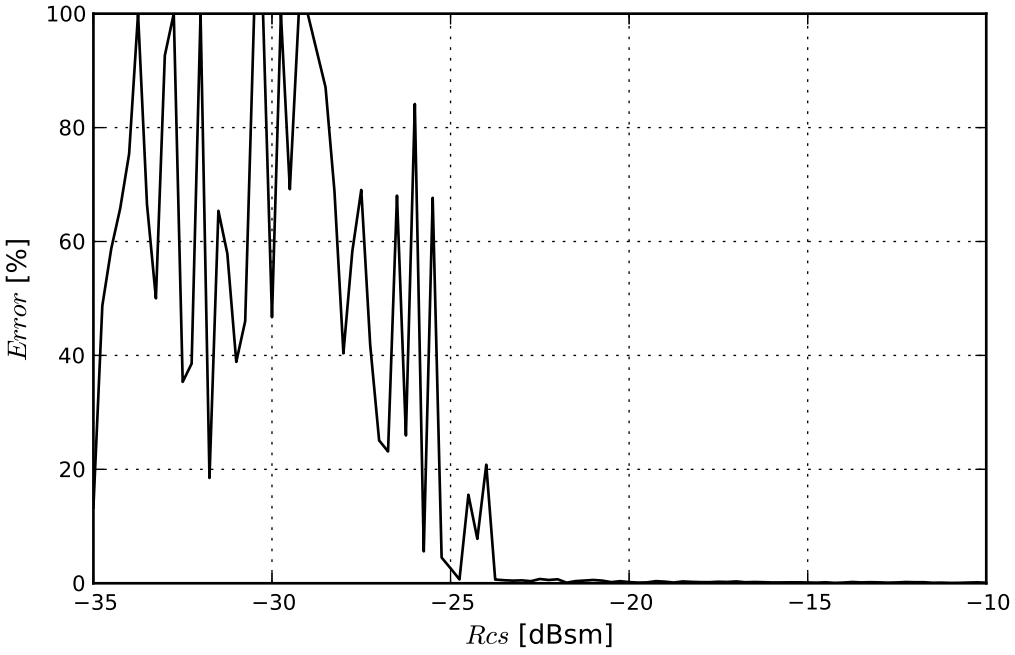

(a) Over Varied RCS

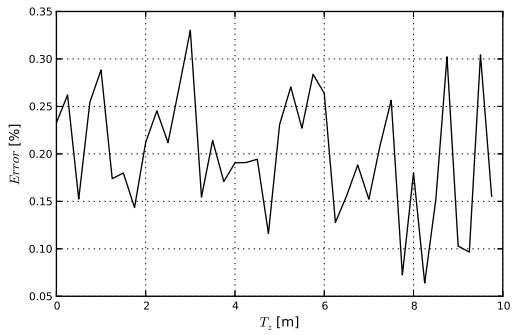

(b) Over Varied T_z

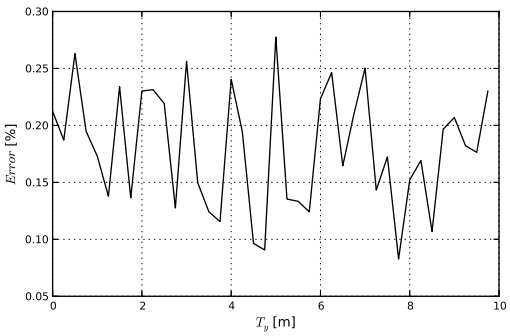

(c) Over Varied T_y

Figure 3.5.4: Median Estimate of F_s

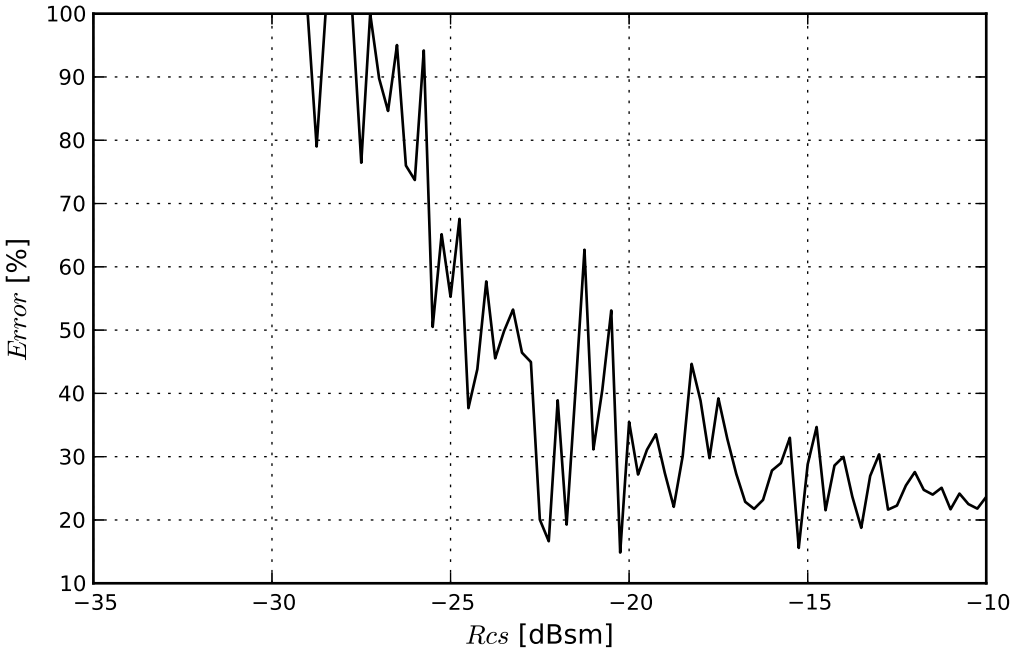

(a) Over Varied RCS

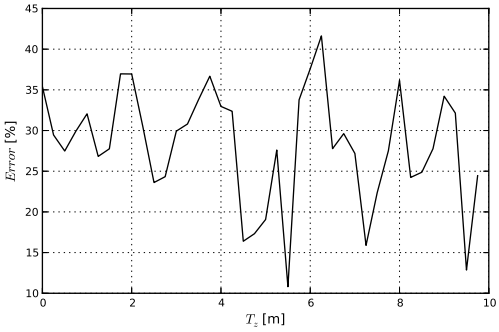

(b) Over Varied T_z

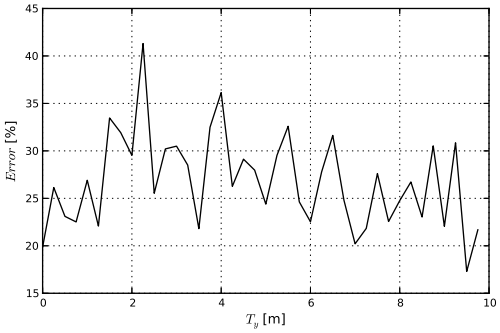

(c) Over Varied T_y

Figure 3.5.5: Median Estimate of A_r

CHAPTER 4

EMPIRICAL MODE DECOMPOSITION AND THE HILBERT-HUANG TRANSFORM

God does not care about our mathematical difficulties.
He integrates empirically.
- Albert Einstein

4.1 Introduction

Having seen the limitations of Fourier analysis when applied to an intensely non-stationary signal such as the radar amplitude track, it was interesting to explore application of Empirical Mode Decomposition (EMD) to the problem. Introduced by Norden E Huang in 1998 [14], this method is singular in its ability to derive basis functions (Intrinsic Mode Functions) from the data set itself rather than pulling from a fixed family of basis functions like the Fourier or Wavelet transform. It is well-suited to decomposition of strongly non-stationary and non-linear data sets owing to its method of defining frequency content based explicitly on local zero crossings in the data rather than fitting to an ensemble of oscillatory functions. This ability to

deal with data sets with non-stationary frequency and large trends made it look like a good choice to use with this type of data set.

4.2 Properties of Intrinsic Mode Functions

An Intrinsic Mode Function (IMF) represents a simple oscillatory mode and is the equivalent of the basis functions used by other transforms such as the Wavelet or Fourier transform. Unlike these other basis functions, IMFs are derived from the data set of interest and are not necessarily related to each other by a parameter change in a generating function. Specifically, any IMF must satisfy two conditions:[14]

1. In the whole data set, the number of extrema and the number of zero crossings must either equal or differ at most by one.

2. At any point, the mean value of the envelope defined by the local maxima and the envelope defined by the local minima is zero.

The first condition is simply formally requiring that the function be oscillatory about zero. The second condition is more specifically requiring the first condition to be met during each cycle. These two criteria essentially require an IMF to have only one frequency, as defined by zero crossings, at any given time during the signal duration.

The IMFs as a set should be able to reconstruct the original signal they were derived from when summed and added to any non-oscillatory residue.

$$X = \sum_{j=1}^{M} C_j + r \tag{4.2.1}$$

X is a set of discrete data, C_j is the j^{th} IMF, r is the non oscillating residual, and M is a number of oscillating modes.

In keeping with their role as a set of basis functions for the data set, the IMFs, taken as a set, should also be orthogonal to each other. Since the IMFs have no analytic or continuous description, we define an index of orthogonality, θ to test numerically how well the set has fulfilled this goal. If we square Equation 4.2.1

$$X^2 = \sum_{j=1}^{M} C_j^2 + 2\sum_{j=1}^{M}\sum_{k=1}^{M} C_j C_k \delta_{j,k} + \sum_{j=1}^{N} C_j r + r^2 \tag{4.2.2}$$

and would like $X^2 = \sum_{j=1}^{M} C_j^2 + r^2$ then we require $\sum_{j=1}^{M}\sum_{k=1}^{M} C_j C_k \delta_{j,k} \to 0$ and $\sum_{j=1}^{M} C_j r \to 0$. We wish our orthogonality condition θ to capture how well our system enforces the condition that the cross-terms sum approached zero. It also bears some mention that the second term that needs to approach zero should do so if the residual r and each mode C_i meet their respective definitions, i.e., since r is a non-oscillating component it simply modulates the envelope of each IMF. If each IMF is oscillatory and has an RMS value near zero then this term should also approach zero. Though this last condition is a bit different from orthogonality [14] defines $C_{n+1} = r$ and defines the orthogonality index in Equation 4.2.3 where we operate on a discrete signals which range over $n = [0 \ldots (N-1)]$.

$$\theta = \sum_{n=0}^{N-1} \left\{ \sum_{j=1}^{M}\sum_{k=1}^{M} \frac{C_j(n) C_k(n) \delta_{j,k}}{X^2(n)} + \sum_{j=1}^{M} \frac{C_j(n) r(n)}{X^2(n)} \right\} = \sum_{n=0}^{N-1} \left\{ \sum_{j=1}^{M+1}\sum_{k=1}^{M+1} \frac{C_j(n) C_k(n) \delta_{j,k}}{X^2(n)} \right\} \tag{4.2.3}$$

Hence θ is simply the cross term of the IMFs normalized by the signal over the duration of the signal where the value of θ should approach zero for an ideal set of IMFs and residual. The Kroncker Delta defined below is used for notational compactness.

$$\delta_{i,j} = \begin{cases} 0 & i = j \\ \\ 1 & i \neq j \end{cases} \tag{4.2.4}$$

Since the normalization is arbitrary the orthogonality index given in Equation 4.2.5 will be substituted so that we do not suffer from divide-by-zero problems in implementation. Also exclusion of the residual from the index does not produce artificial increase in θ when the frequency changes dramatically over the course of the signal.

$$\theta = \sum_{j=1}^{M} \sum_{k=1}^{M} \delta_{j,k} \left\{ \frac{\sum_{n=0}^{N-1} C_j(n) C_k(n)}{\sum_{n=0}^{N-1} X^2(n)} \right\} \tag{4.2.5}$$

4.3 Sifting and Stopping Criteria

The sifting process as described in [14, 15, 16] is the process of deriving a set of IMFs from a data set. To explain this process an example of decomposition of the simple two-tone discrete data set

$$X(n) = \sin\left(2\pi 3\left({}^{nT}/_{N}\right)\right) + \frac{1}{2}\sin\left(2\pi 13\left({}^{nT}/_{N}\right)\right) \tag{4.3.1}$$

where T is the period , $n = [0..(N-1)]$ and $X(n)$ is shown in Figure 4.3.1.

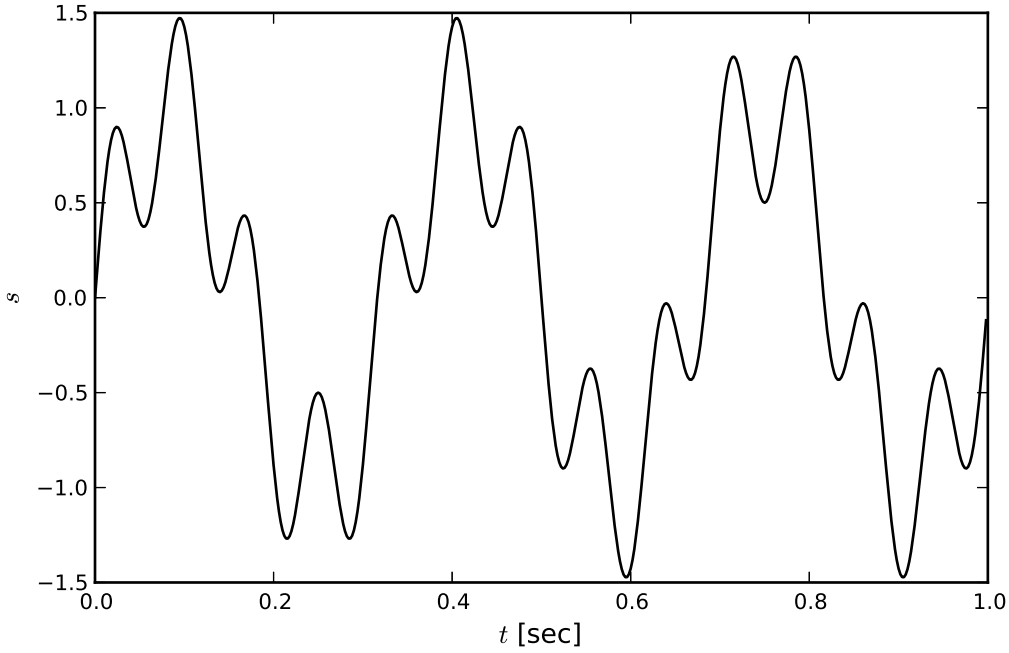

Figure 4.3.1: Two Tone Example

The first step is to obtain a list of local minima and maxima in the data set. This can easily be accomplished by stepping through the array from $n = 1$ to $n = 498$ and storing a list of points that satisfy the criteria $X(n-1) > X(n) < X(n+1)$ for local minima and $X(n-1) < X(n) > X(n+1)$ for the local maxima. Apply this to the example data set we obtain the maxima and minima show in figure 4.3.2a. The set of local maxima and minima can be used to interpolate an upper envelope u_0 and lower envelop l_0 respectively through the use of a cubic spline which is shown in figure 4.3.2b. Once these envelopes have been created their mean $m_0 = \frac{u_0+l_0}{2}$ can be found which is shown in figure 4.3.2c. Once this mean is defined we can use to attempt to find the first IMF by forming the difference between the data set and the mean designating it $h_0 = X - m_0$. This result is shown in figure 4.3.2d.

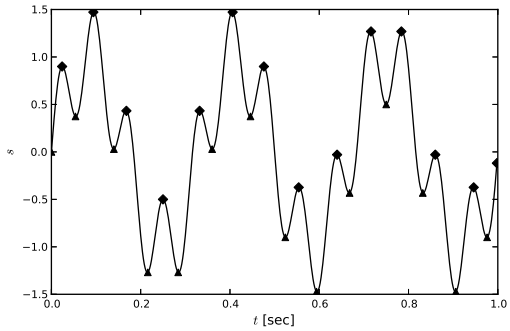

(a) Maxima (diamonds) and Minima (triangles)

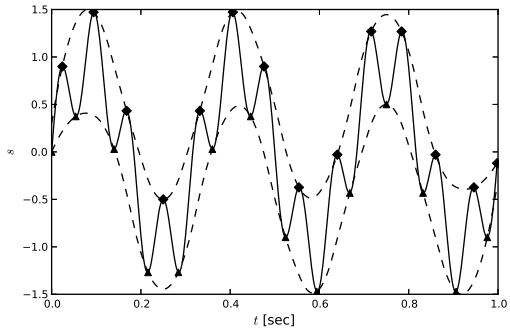

(b) Envelopes $u_1$and l_1

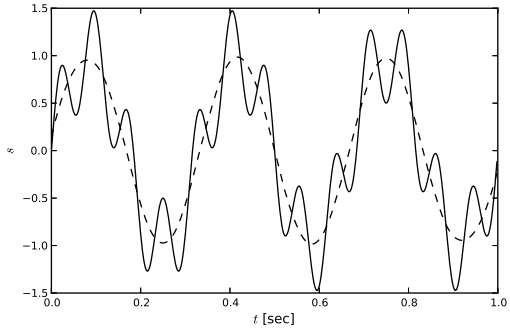

(c) Mean Envelope

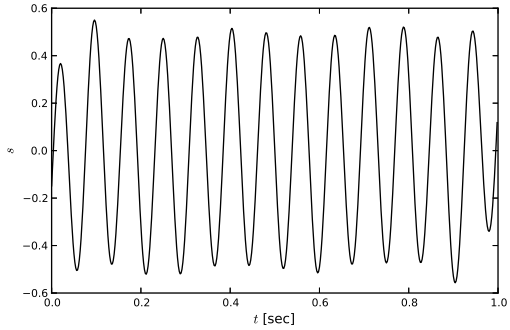

(d) h_1

Figure 4.3.2: Sifting Step

Ideally, h_0 would be the first IMF but in practice the process can have undesirable overshoot or the initial subtraction can reveal new extrema. To deal with this, the signal is sifted repeatedly by forming a mean of h_0 in the same manner as the first step, and proceeds to refine the IMF more and more by producing $h_{0,k} = h_{0,(k-1)} - m_{0,k}$. This process is repeated until $h_{0,k}$ has not changed significantly from the previous iteration; this is stopping criteria and is typically accomplished by terminating the

sifting process once the following criteria is met:

$$\frac{\sum_{n=0}^{N-1}\left|\left(h_{0,(k-1)}(n)-h_{0,k}(n)\right)\right|^2}{\sum_{n=0}^{N-1}\left|h_{0,(k-1)}(n)\right|^2} < S_{lim} \tag{4.3.2}$$

where $S_{lim} = 0.005$ was used. Repeated sifting of the example signal quickly reaches this limit and the final iteration of $h_{0,k}$ is saved as the first IMF $IMF_0 = c_0 = h_{0,k}$. This IMF is subtracted from that data and an intermediate residual is formed $r_0 = X - c_0$, which is then used in place of X above and the procedure repeated. To determine when all of the IMFs have been found, each residue is checked to determine if it no longer has oscillatory components. This is accomplished by testing it against the IMF criteria in section 4.2; if it fails these criteria then the final residual has been found. This residual is typically a dc offset of monotonic trend in the data. Figure 4.3.3 shows the result of sifting the example signal, the two tones have clearly been isolated and the residual is small.

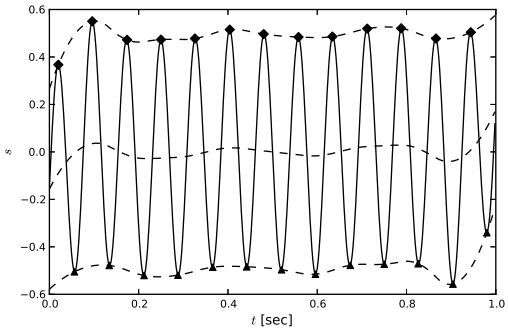

(a) First IMF$c_0 = h_{0,1}$

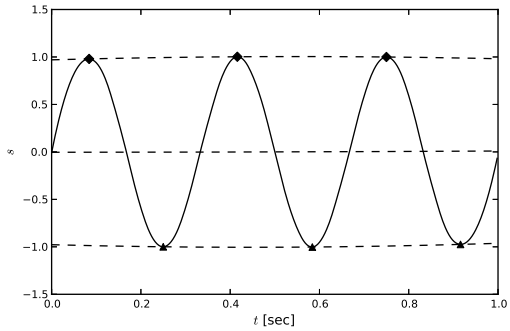

(b) Second IMF$c_1 = h_{1,1}$

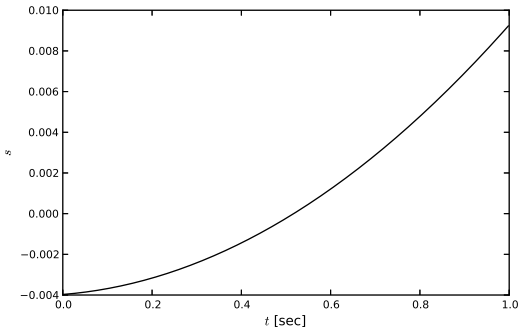

(c) Residue r

Figure 4.3.3: Example IMFs and Residue

4.4 Hilbert Huang Transform (HHT)

Now that we have decomposed the data into a set of IMFs we can use this to attempt to gain insight into the data. Since each IMF should have only one characteristic frequency at any given time, it is natural to look at the frequency and amplitude of each IMF as a function of time or sample number. Any time series can be made into an analytic or complex function through the use of the Hilbert transform, allowing

use to take the real signal X and transform it into a complex signal

$$Z = X + j\hat{X} \tag{4.4.1}$$

where $\hat{X}$is the Hilbert transform of X [17]

$$\hat{X}(t) = \frac{1}{\pi}\int_{-\infty}^{\infty}\frac{X(t)}{t-\tau}d\tau \tag{4.4.2}$$

Equation 4.4.2 is a continuous definition that must be approximated to be used on discrete data sets. Commonly FFT and filter methods are used to approximate the Hilbert transform but both suffer from bandwidth restrictions and ripple. If we restrict ourselves to transforming IMFs that are by definition oscillatory, the discrete approximation to the Hilbert transform may often be meaningful. Once we have formed the complex signal Z we can apply the definition of instantaneous frequency in [14] and [13]

$$\omega = \frac{d\theta(t)}{dt} \tag{4.4.3}$$

by estimating the instantaneous phase of the signal with

$$\theta(t) = \arctan\left(\frac{\hat{X}(t)}{X(t)}\right) \tag{4.4.4}$$

and the instantaneous amplitude with

$$a(t) = \sqrt{X^2(t) + \hat{X}^2(t)} \tag{4.4.5}$$

for the example signal we can see the estimate of ω over time in figure 4.4.1a is constant for both IMFs as is $a(t)$ in Figure 4.4.1b. This behavior corresponds to the underlying signal characteristic nicely for this simple example. Finally, we attempt to form a plot similar to the STFFT spectrogram in Figure 4.4.1c by plotting a line with varying color that corresponds to amplitude, frequency in the vertical axis, and time or sample in the horizontal axis. When the signal is decomposed with EMD into IMFs which are then analyzed for instantaneous frequency and amplitude, the final result will be referred to as the Hilbert Huang Transform or HHT.

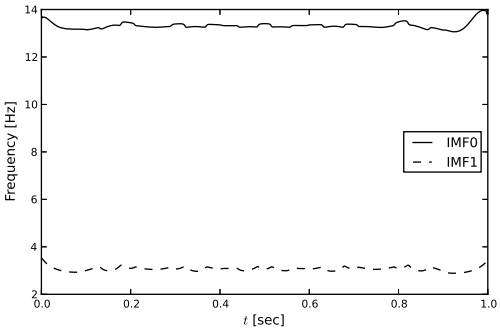

(a) Mono-frequencies for each IMF

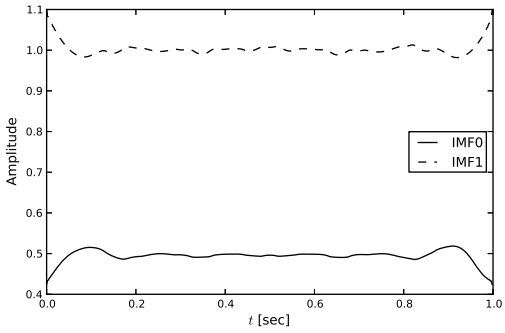

(b) Mono-frequency Amplitude for each IMF

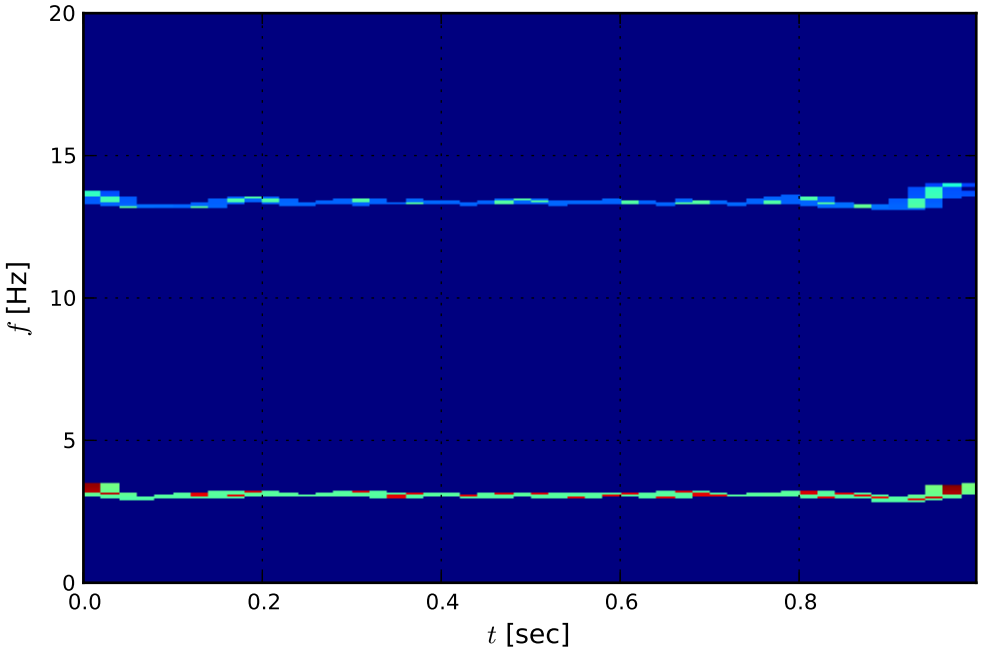

(c) HHT

Figure 4.4.1: HHT of Example

4.5 EMD of the radar track

The noise-free version of the simulated received signal shown in Figure 2.4.1 was decomposed using EMD into a set of IMFs and the result is shown in Figure 4.5.1.

The results shown in Figure 4.5.1 exhibit very clear separation of the modes allowing clear association of each IMF with the basic $1/r^4$ power roll-off, multipath propagation factor, or the roll-induced flutter. Clear as they are, there was some coupling between the $1/r^4$ roll-off and the multipath modes. Progressing on and looking at the HHT of the signal in Figure 4.5.2, some edge effects are present, but the simultaneous tone and chirp behavior are easily seen.

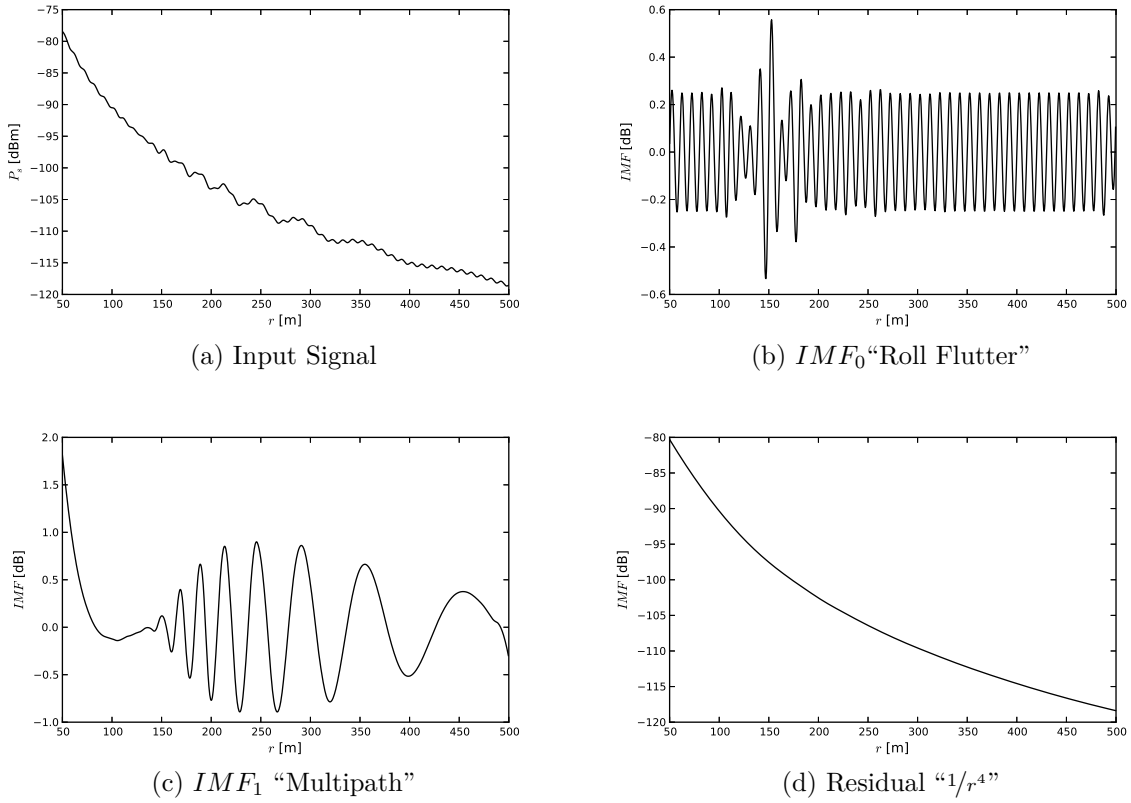

(a) Input Signal

(b) IMF_0"Roll Flutter"

(c) IMF_1 "Multipath"

(d) Residual "$1/r^4$"

Figure 4.5.1: EMD Derived IMFs of Noise Free Signal

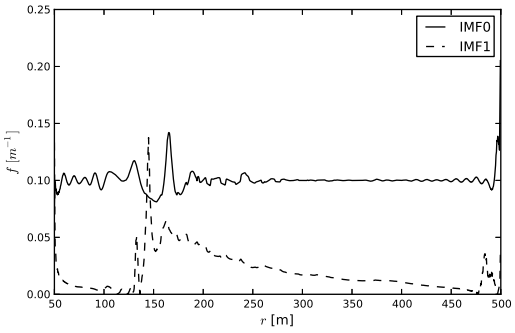

(a) Mono-frequencies for each IMF

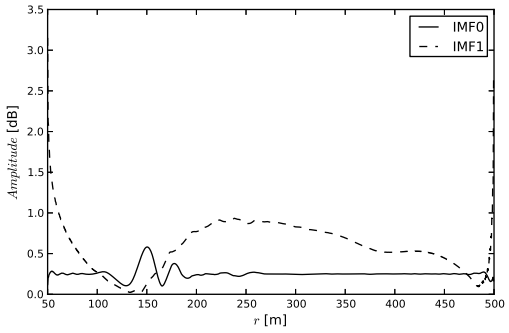

(b) Mono-frequency Amplitude for each IMF

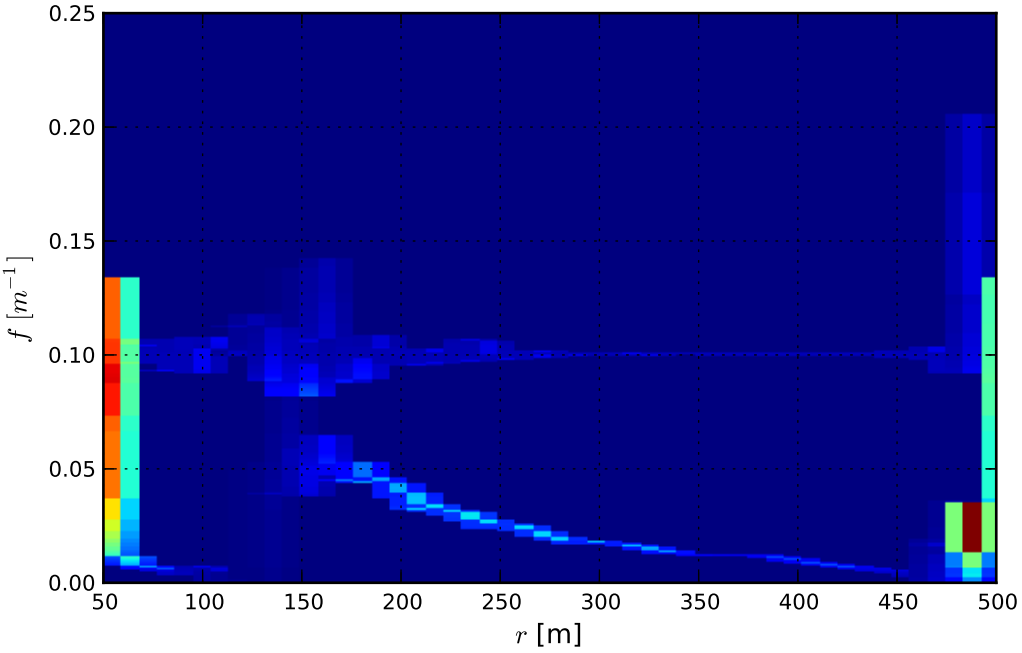

(c) HHT

Figure 4.5.2: HHT of Clean Signal

Once noise is added and the signal shown in Figure 2.5.2 was decomposed, the results changed dramatically. It appears that decomposition in the presence of noise results in over sifting, which was exacerbating boundary effects which resulted in highly non-physical IMFs. These IMFs are very dependent on the particular real-

ization of noise. The realization shown in Figure 4.5.3 produced a reasonable residual but this is not always the case. Progressing on and looking at the HHT of the signal in Figure 4.5.4, very little of the characteristics of the signal are discernible. This inconsistency of the transform result can be quantified by looking at the orthogonality index θ, one thousand noise realizations of the baseline were decomposed and only 32% had orthogonality indicies less than 1.0. In addition the number of IMFs found varies between 6 and 8, Figure 4.5.5 summarizes the results.

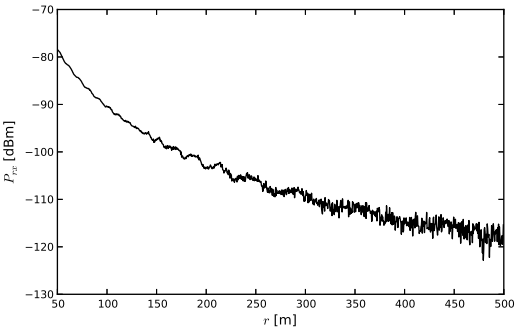

(a) Input Signal

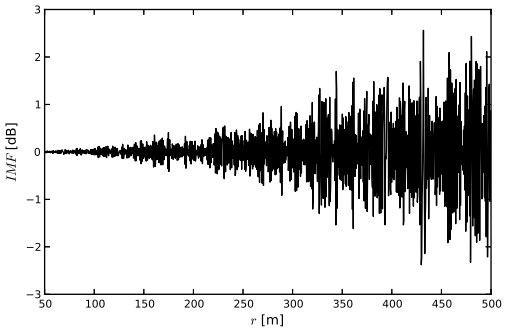

(b) IMF_0

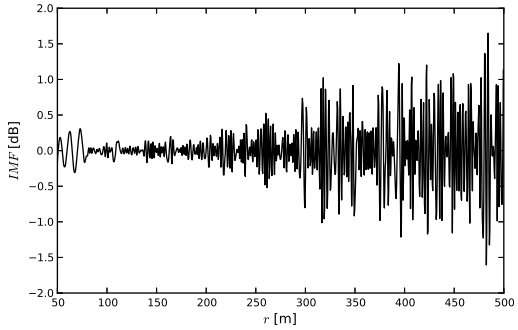

(c) IMF_1

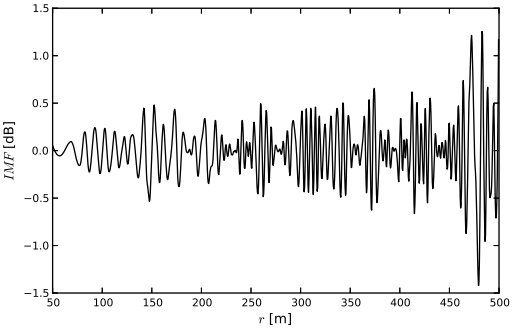

(d) IMF_2

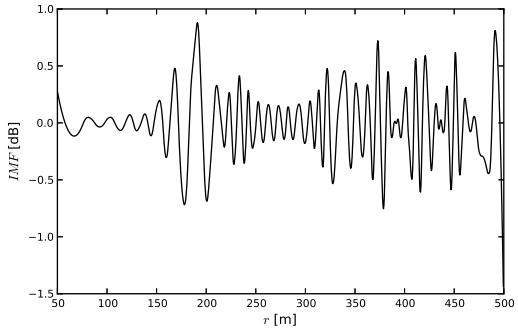

(e) IMF_3

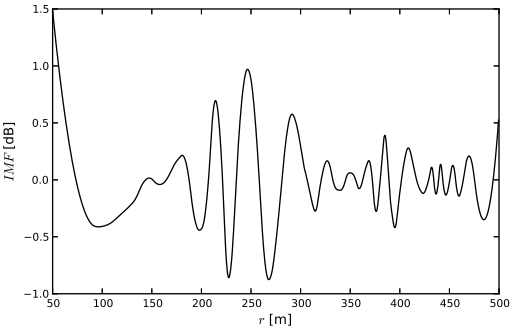

(f) IMF_4

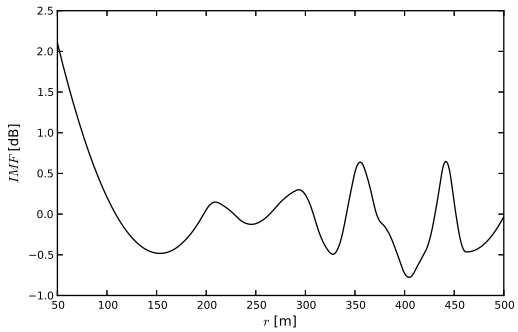

(g) IMF_5

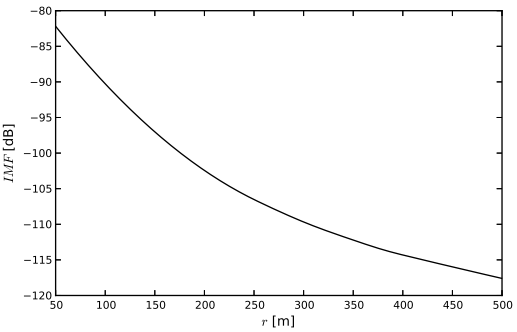

(h) Residual

Figure 4.5.3: EMD derived IMFs of Signal with Noise

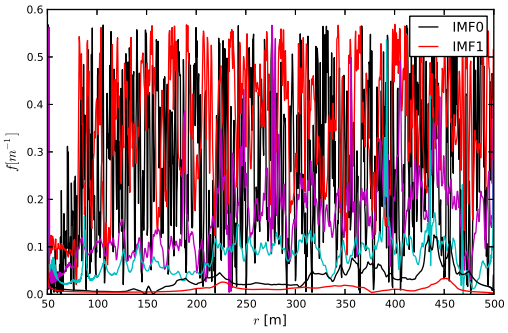

(a) Mono-frequencies for each IMF

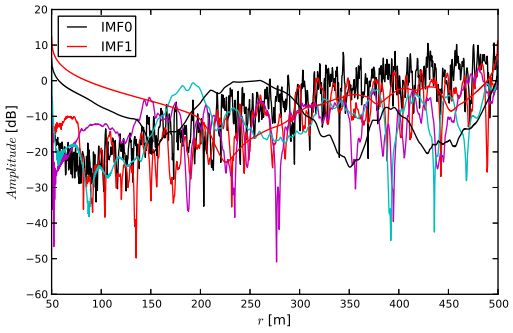

(b) Mono-frequency Amplitude for each IMF

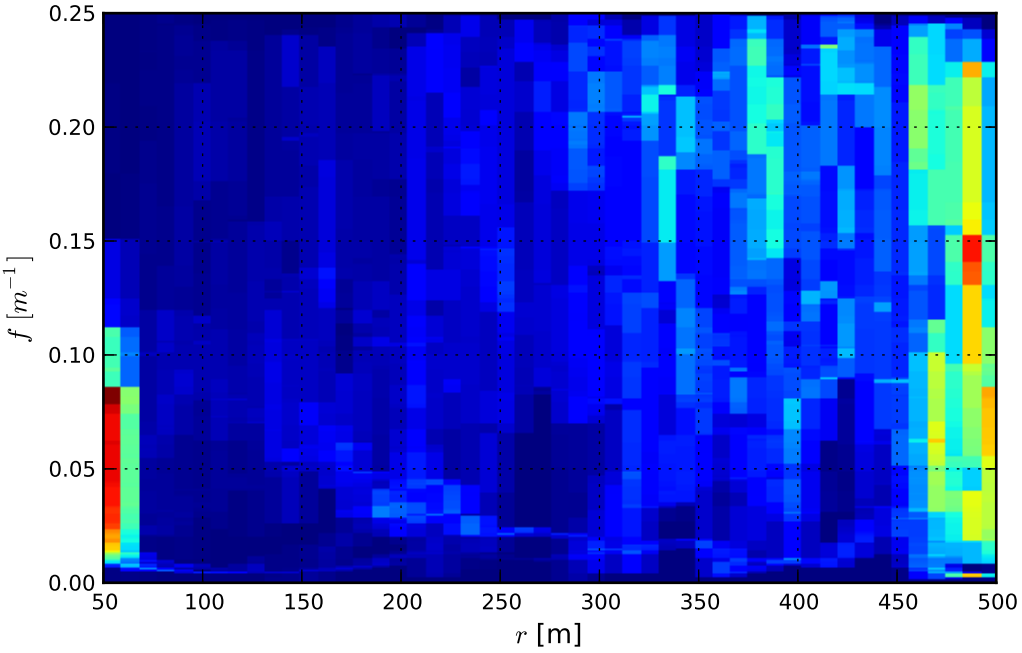

(c) HHT

Figure 4.5.4: HHT of Signal with Noise

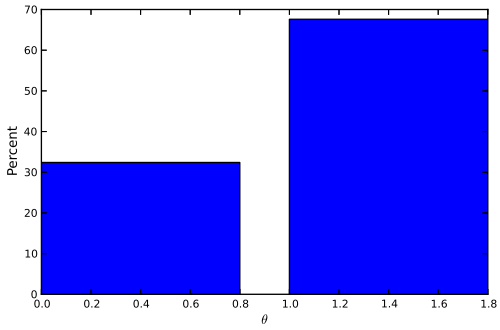

(a) Orthogonality Index $0.0 > \theta > 0.1$ or $\theta \geq 0.1$

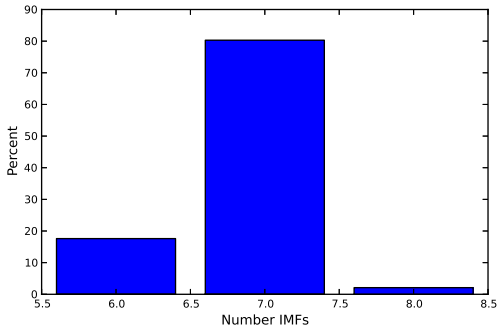

(b) Number of IMFs Found

Figure 4.5.5: Transform Quality

CHAPTER 5

A PRIORI MODE DECOMPOSITION

Everything should be made as simple as possible, but not simpler.
- Albert Einstein

5.1 Introduction

The strength of EMD is that no knowledge of the underlying signal is required to decompose the signal. This is a significant asset when attempting to decompose signals where there is an incomplete understanding of the underlying process, such as with the sunspot cycle or turbulent pressure data.[18] In the case of the radar signal considered in this thesis, the governing equations of the components of the signal are known a priori. It seems reasonable that we should be able to use that information to form a better decomposition of the signal.

In essence, the EMD method sifts high-frequency information from the signal, assigns it as an IMF, and then subtracts it from the signal. This process is then repeated until no oscillatory data remains. Inspired by the EMD method, an algorithm was developed to attempt to fit a model of each underlying process, form a signal for this "a priori mode function" (AMF) and then subtract it from the signal. This

process is repeated until all the known modes have been estimated and removed. The residual should then consist of unmodeled dynamics and noise.

The most straightforward method is to look at the residual between the signal and a mode function

$$g\left(x,\vec{p}\right)=R_{i-1}\left(x\right)-m_i\left(x,\vec{p}\right) \tag{5.1.1}$$

where $R_i\left(x\right)$ is the current signal, $m_i\left(x,\vec{p}\right)$ is the mode constructed with parameters $\vec{p}$ over x. A cost function such as the ℓ_1 norm then assigned and a minimization program is run

$$\min\sum_{x=x_{min}}^{x_{max}}\left|g\left(x,\vec{p}\right)\right|=\min\,\ell_{1g} \tag{5.1.2}$$

the $\vec{p}$ that forms the minimum is then assigned as a mode

$$a_i\left(x\right)=m_i\left(x,\vec{p}_{min}\right) \tag{5.1.3}$$

and subtracted from the signal.

$$s_i\left(x\right)=R_{i-1}\left(x\right)-a_i\left(x\right) \tag{5.1.4}$$

At this point we already diverge from EMD; EMD estimates the IMFs using the envelope of the signal. This has the effect of estimating the mode with the highest frequency content first and removing it in roughly decreasing order of frequency until a residual is left. In order for above algorithm to succeed, $g\left(x\right)$ must have a minimum. This is made more likely by assigning $m_i\left(x,\vec{p}\right)$ that estimates the local mean or trend

of the signal. To make clear why this important step is necessary, let us consider the simple tone with a linear trend

$$s(t) = 2t + \sin(2\pi f t) \tag{5.1.5}$$

where $f = 5$ and $0.0 \leq t < 1.0$ then the result is shown in Figure 5.1.1.

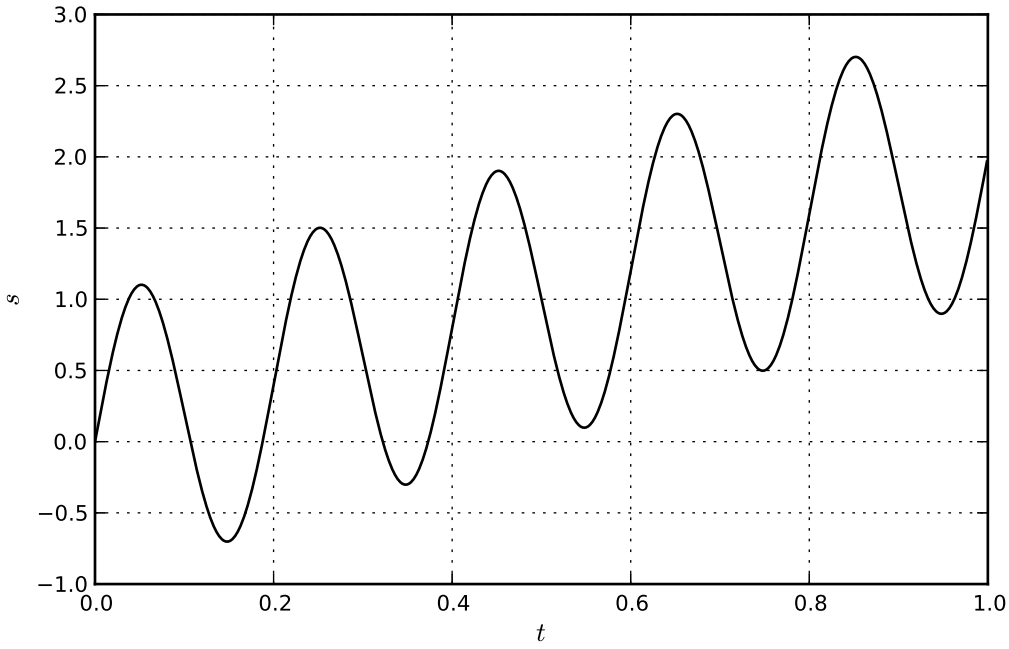

Figure 5.1.1: Example Signal

If we go on to form the cost function $g(t, f) = s(t) - \sin(2\pi f t)$ and generate the value of the ℓ_1 norm over frequency we would get the solid line in Figure 5.1.2 which would have directed an unconstrained minimization program to identify $f = 0.3$ as the global minimum. Even if we had constrained the search near the value of $f = 5.0$, the program would still have chosen either $f = 5.3$ or $f = 4.7$. The reason

for this can be seen in Figure 5.1.3 where comparison of $g(t, 5.0)$ in (a) and $g(t, 5.3)$in (b) clearly show why the ℓ_1 norm fails to find the true fit for this case. If the trend-line is removed first, then the behavior shown by the dashed line in Figure 5.1.2 is achieved which would clearly choose the proper answer of $f = 5.0$. This simple example illustrates the importance of removing the low-frequency trend information before attempting to fit to higher frequency oscillatory modes.

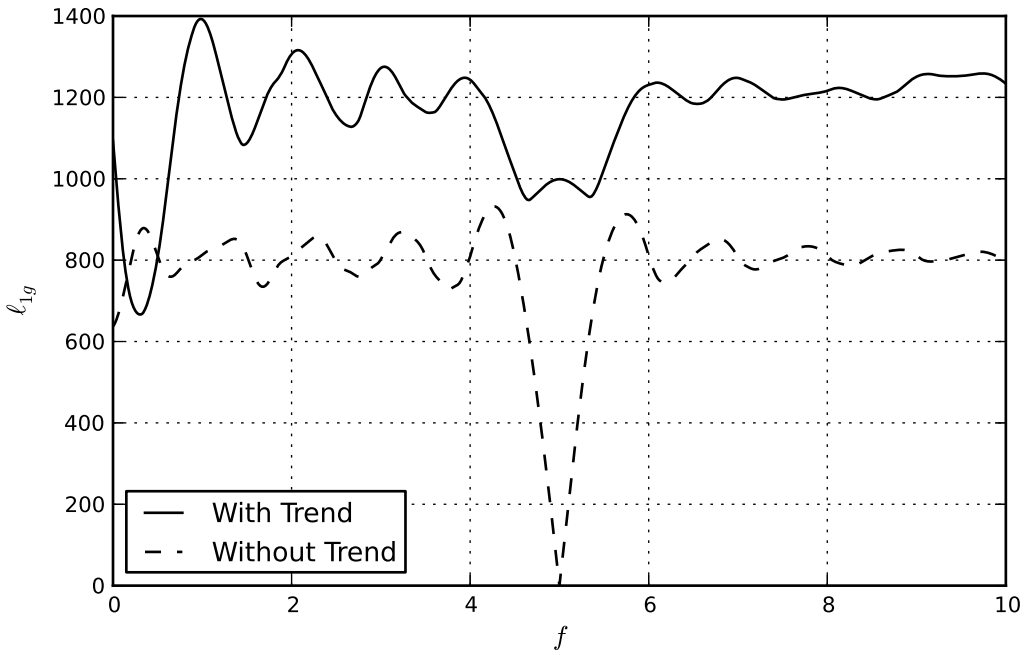

Figure 5.1.2: ℓ_1 Norm vs Frequency with and without Trend

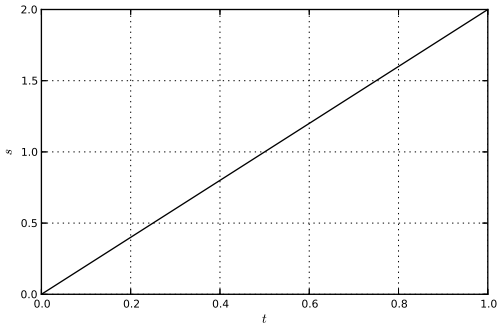

(a) $g\left(t, f = 5.0\right)$

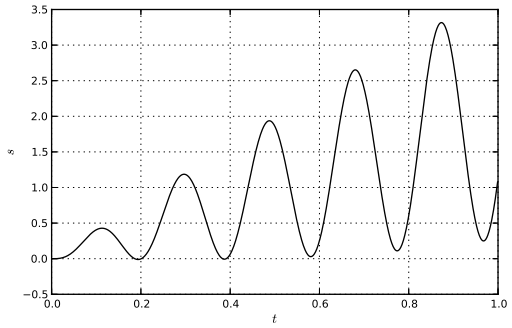

(b) $g\left(t, f = 5.3\right)$

Figure 5.1.3: $g\left(t, f\right)$

5.2 Description of the Algorithm

The algorithm can be described by the following 6 steps:

1. The known modes should be arranged by inspection from lowest frequency content to highest $m_0\left(x, \vec{p}\right) \ldots m_n\left(x, \vec{p}\right)$

2. Set $k = 0$ and designate the input signal $R_0\left(x\right)$

3. Fit $m_k\left(x, \vec{p}\right)$ to $R_k\left(x\right)$ to form an estimate $\hat{\vec{p_k}}$ of the mode parameters

4. Form the first IMF, $IMF_k = m_k\left(x, \hat{\vec{p_k}}\right)$

5. Form the working residual $R_{k+1}\left(x\right) = R_k\left(x\right) - IMF_k$

6. Set $k = k + 1$ and repeat at step 3 until all known modes are complete

5.3 Example

To explain the algorithm more fully, an example decomposition of the radar track signal generated with radar parameters from Table 2.1 as well as the target parameters shown in Table 2.2 and terrain parameters in 2.3 will be performed. Table 5.1 summarizes the key parameters that will be considered in this section. It is assumed that the radar data collected is in a test range environment, so the radar operating parameters and flight path is known via the normal radar range and bearing operation. Thus R_z, T_y, T_z are known but the rest of the parameters must be estimated from the amplitude return data shown in Figure 2.5.2.

Parameter	Truth
σ_{rcs}	$-15.0\,dBsm$
α	$0.24\,Np/m$
σ_h	$40.00\,mm$
A_r	$0.2\,dB$
F_s	$0.10\,{}^1\!/_m$
R_z	$3.0\,m$
T_y	$1.0\,m$
T_z	$2.0\,m$

Table 5.1: Example Parameters

5.3.1 Arrangement of Modes

Step one is to arrange the a priori modes into ascending order of frequency content. The overall amplitude return signal is composed of the r^{-4} roll off in the radar range equation, the chirped frequency pulse of the multipath components, the steady tone of the roll flutter, and noise.

Since the radar range equation has no oscillating components it is assigned first. The equation is given in Equation 2.2.1 and used as m_0 where the only unknown parameter to estimate is σ_{rcs}:

$$m_0\left(r, \langle \sigma_{rcs} \rangle\right) = \frac{P_{tx} G_r G_t \lambda^2 \sigma_{rcs}}{(4\pi)^3 r^4} \tag{5.3.1}$$

Next, the multipath signal described in Equation 2.3.20 is used as m_1 where the unknown parameters are σ_h, and α. Since the target track and is known $\theta_g\left(r, T_x, T_z, R_z\right)$ and the rest of the radar parameter such as P_{tx} and λ are constant.

$$\begin{aligned} m_1\left(r, \langle \sigma_h, \alpha \rangle\right) = e^{jl_d 2\pi/\lambda} + 2R_{\rho o}\left(\theta_g\right) \rho_s\left(\theta_g, \sigma_h\right) A\left(\theta_g, \sigma_h, \alpha\right) e^{jl_a 2\pi/\lambda} \\ + R_o^2\left(\theta_g\right) \rho_s^2\left(\theta_g\right) A^2\left(\theta_g\right) e^{jl_c 2\pi/\lambda} \end{aligned} \tag{5.3.2}$$

The roll-induced amplitude flutter described in Equation 2.4.1 is used as m_2, where the unknown parameters are the amplitude A_r, frequency F_s, and phase ϕ.

$$m_2\left(r, \langle A_r, F_s, \phi \rangle\right) = A_r \sin\left(2\pi r F_s + \phi\right) \tag{5.3.3}$$

5.3.2 Range Equation

Once the modes have been ordered, steps 2-5 can be performed. The signal shown in Figure 2.5.2 is assigned to R_0 and then fit to $m_0\left(r, \langle \sigma_{rcs} \rangle\right)$ using the downhill simplex

algorithm. This resulted in an estimate of RCS $\hat{\sigma}_{rcs} = -15.0\,dBsm$ which is then used to generate a mode function IMF_0 shown overlaid onto R_0 in Figure

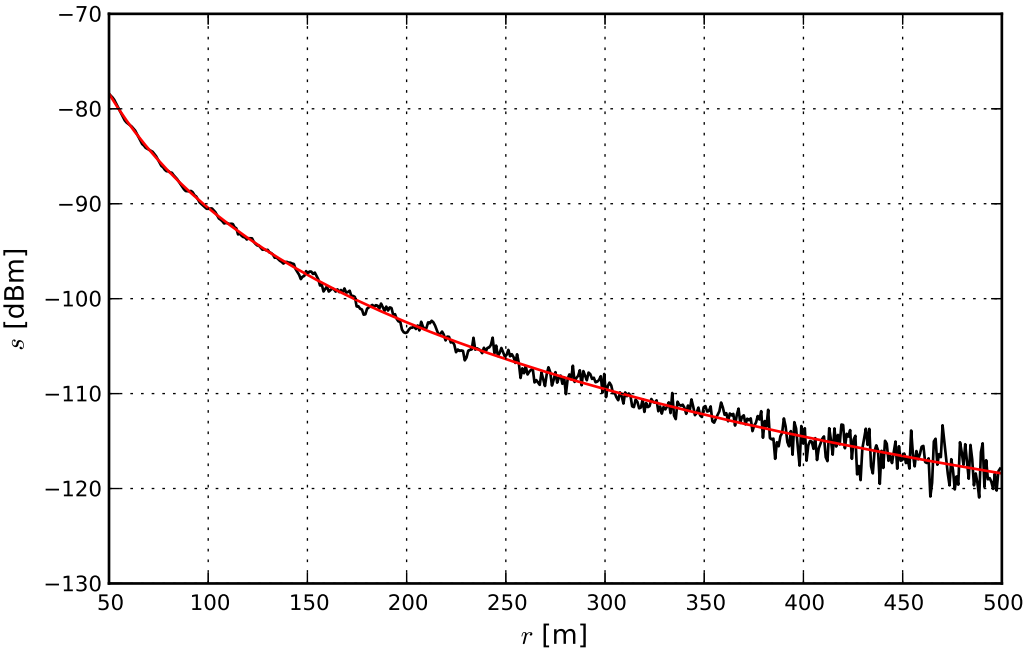

Figure 5.3.1: Range Equation Fit

5.3.3 Multipath

After the first mode estimate is made, steps 2-5 can be performed again for the second mode. IMF_0 is subtracted from R_0 to form R_1 which is then fit to $m_1\left(r, \langle \sigma_h, \alpha \rangle\right)$ using the same downhill simplex algorithm used by the previous step. This resulted in an estimate of the surface roughness $\hat{\sigma}_h = 39.86\,mm$, and attenuation rate $\hat{\alpha} = 0.26\,Np/m$ which is then used to generate the mode function IMF_1, shown overlaid onto R_1 in Figure 5.3.2.

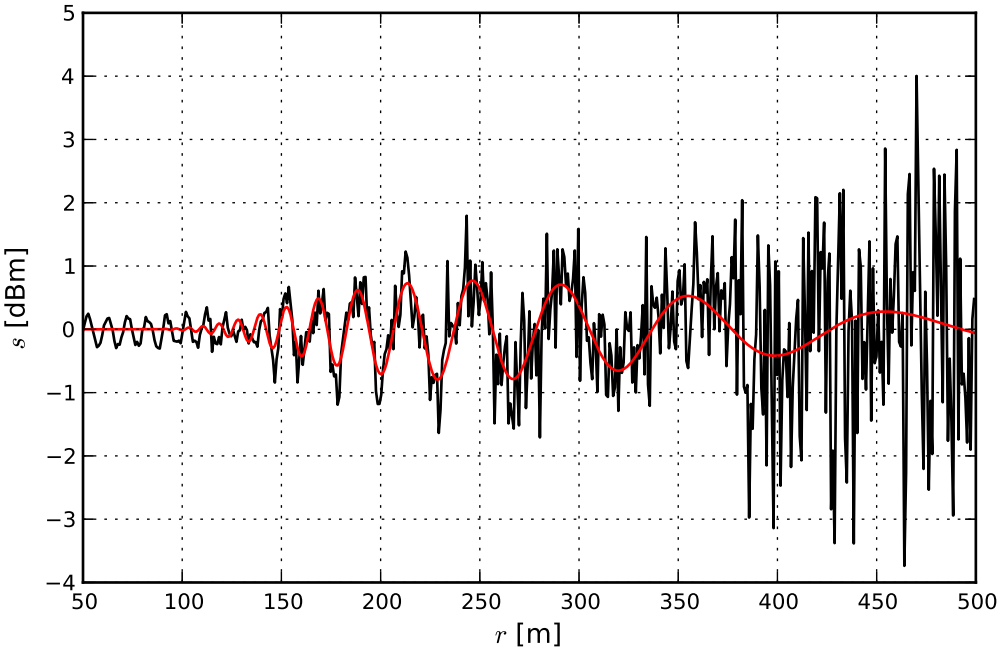

Figure 5.3.2: Multipath Fit

5.3.4 Roll Induced Flutter

After the second mode estimate is made, steps 2-5 can be performed again for the third and final mode. IMF_1 is subtracted from R_1 to form R_2, which is then fit to $m_2\left(r, \langle A_r, F_s, \phi \rangle\right)$. Since this is a simple sinusoidal signal, Fourier methods are employed. The result is an estimate $\hat{A}_r = 0.10\,dB$, and $\hat{F}_s = 0.25\,1/m$ which is shown overlaid onto R_2 in Figure 5.3.3.

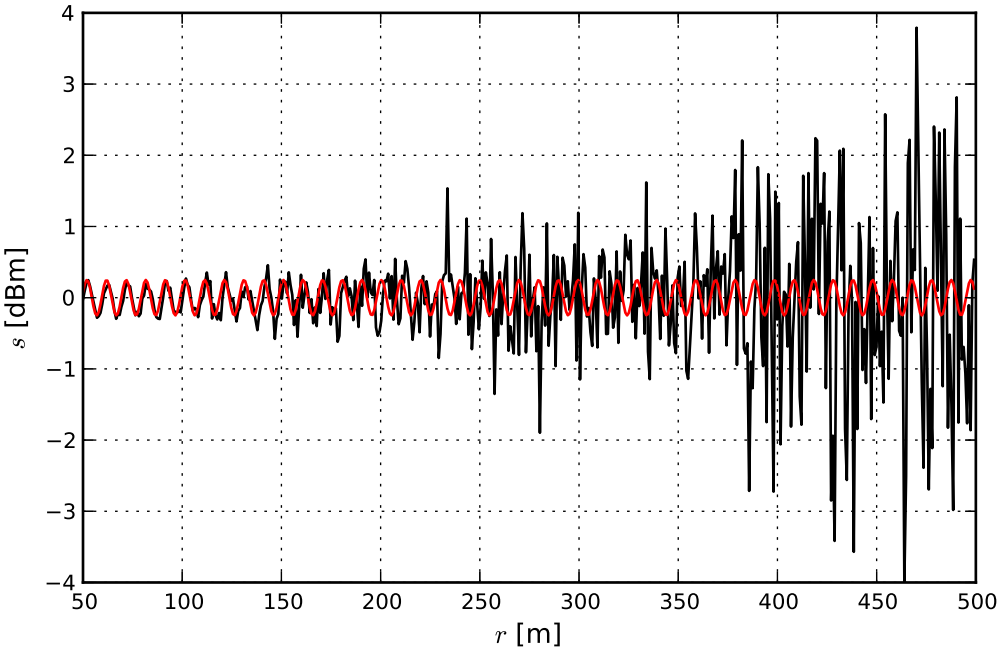

Figure 5.3.3: Roll Flutter Fit

5.3.5 Residual

In this case, the residual shown in Figure 5.3.4 consists primarily of the system noise. Since the log power signal was decomposed to allow the other signal features to be a linear combination of modes, the noise appears to be non-stationary.

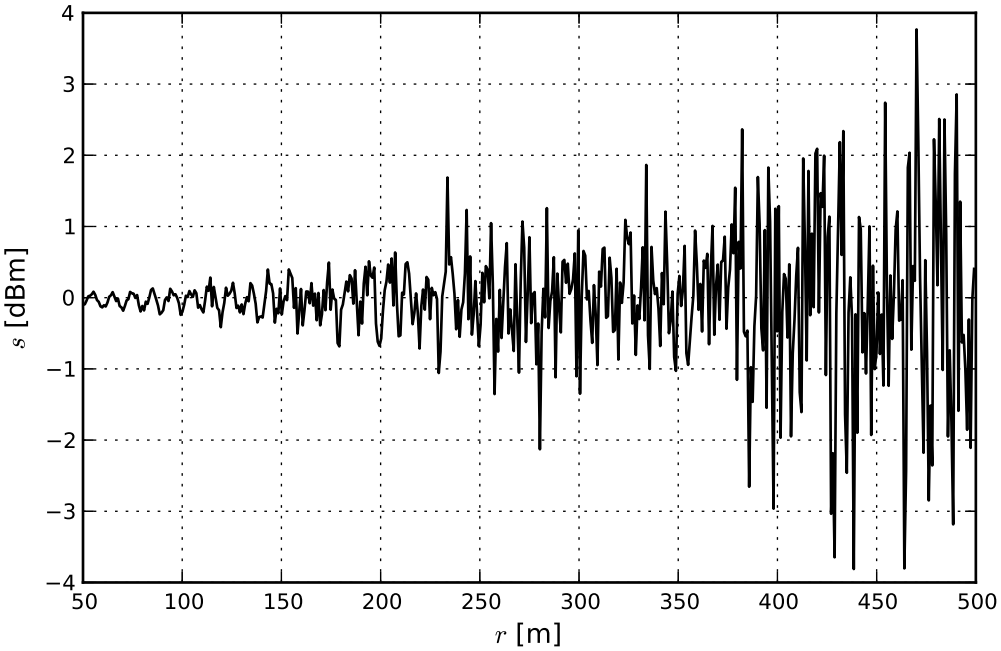

Figure 5.3.4: Residual

5.4 Sensitivity

To determine the robustness of the method against different system parameters, first the signal was generated using the values in the previous section with one parameter swept in over a range. At each parameter value the method was applied to 10 different noise realizations and the median percentage error was recorded. First the target RCS (σ_{RCS}) was varied from -35 to -10 dBsm. The median error in the estimates of the system parameters are shown in Figure 5.4.1. In this figure, it can be seen that the estimation of σ_{RCS} is better than 3% throughout the range. Estimation of surface parameters σ_h and α require cross sections greater than $-20dBsm$, and estimation of the roll rate requires a cross section greater than $-30dBsm$.

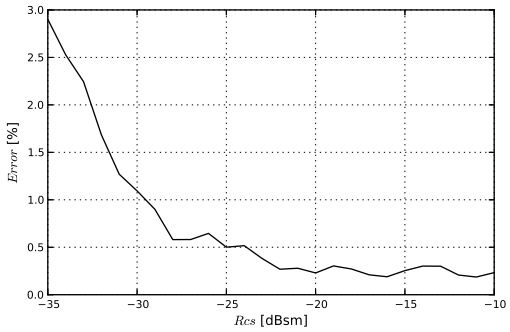

(a) σ_{RCS}

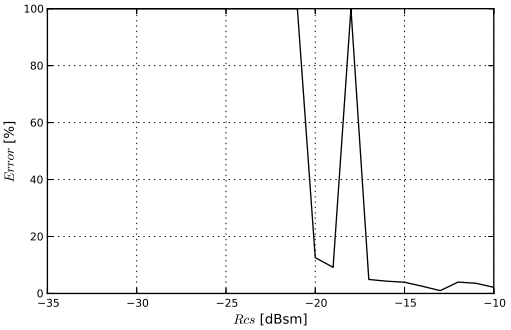

(b) σ_h

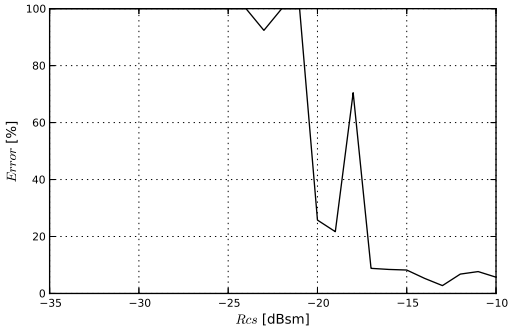

(c) α

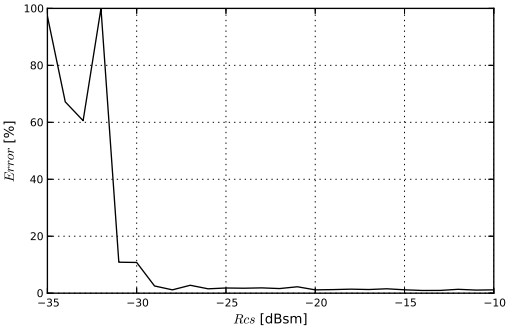

(d) F_s

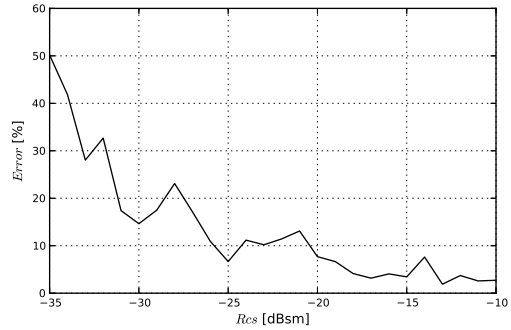

(e) A_r

Figure 5.4.1: Parameter Estimation Error vs Target RCS

Next, the target altitude and cross range was swept from 0 to 10m, and the results shown in Figures 5.4.2 and 5.4.3. In these plots we see low to moderate estimation errors spread uniformly over the range. Combined with the previous RCS

sweep, this suggests the algorithm is not "tuned" for a particular realization or point in parameter space. Parameter estimation success seemed to be more dependent on target altitude than cross range.

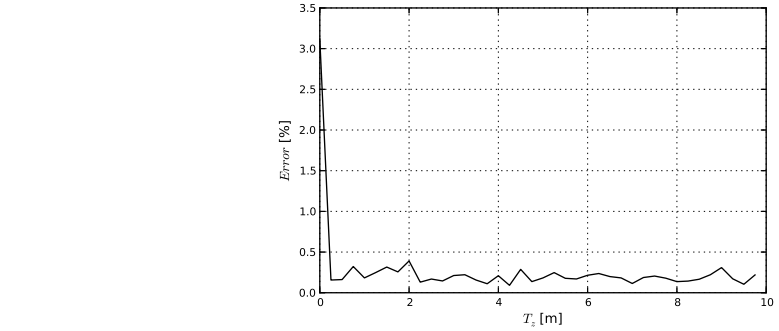

(a) σ_{RCS}

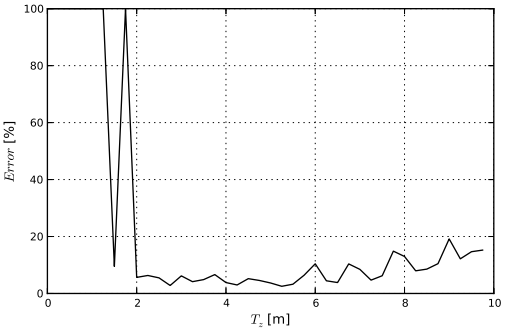

(b) σ_h

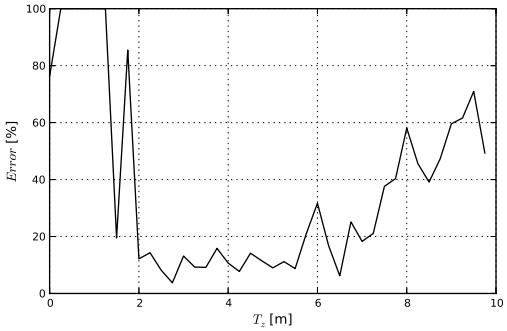

(c) α

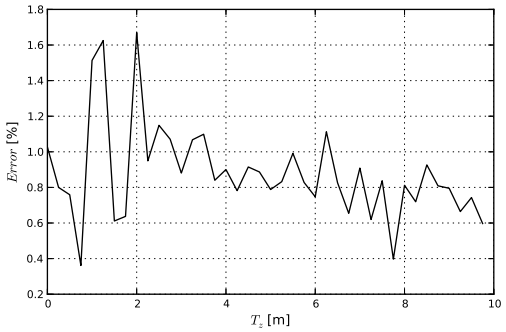

(d) F_s

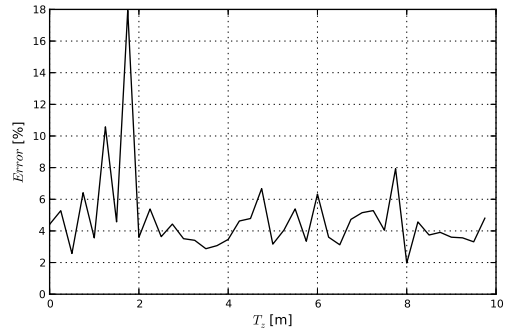

(e) A_r

Figure 5.4.2: Parameter Estimation Error vs Target Altitude

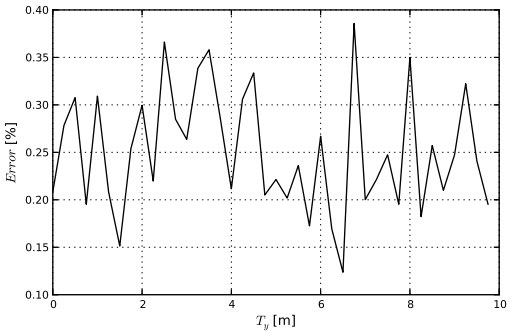

(a) σ_{RCS}

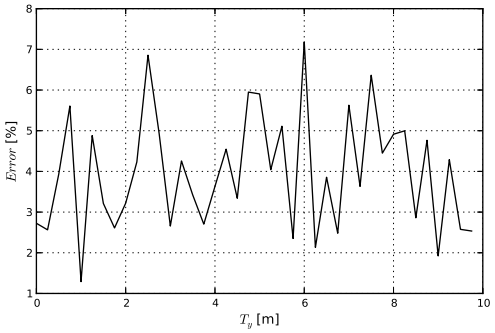

(b) σ_h

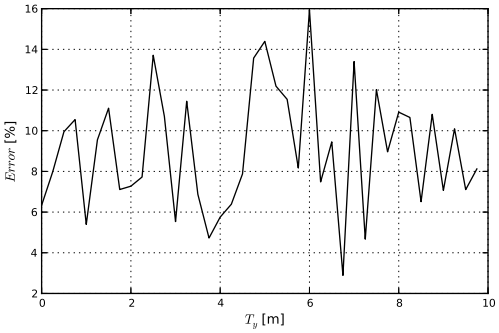

(c) α

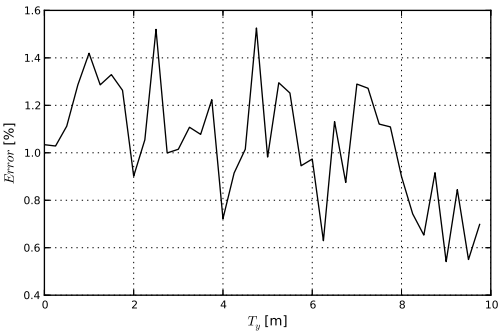

(d) F_s

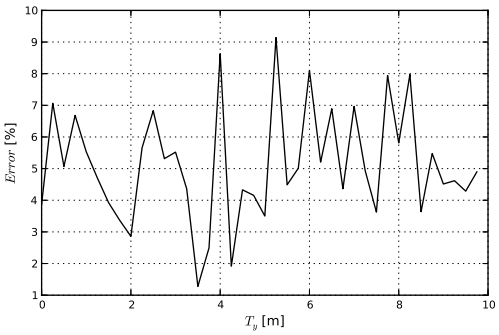

(e) A_r

Figure 5.4.3: Parameter Estimation Error vs Target Cross Range

CHAPTER 6

CONCLUSION

Engineers aren't boring people, we just get excited over boring things.
- Annonymous

6.1 Overview

In this thesis, a detailed amplitude model of a target over rough flat terrain was developed. This amplitude track data was then analyzed with Fourier methods which had some success identifying the roll rate of the target but gave no insight into the multipath behavior. EMD was then investigated which had some success decomposing a pristine track but did not work in the presence of noise. Finally, EMD was used as inspiration to develop a method of successive regression and fitting to the data dubbed AMD. AMD was applied not only to a single simulated environment but was applied in Monte Carlo fashion to a large portion of parameter space which showed it to be effective and robust to changes in the modeled system parameters.

At a very high level, EMD and AMD are similar and part of the greater family of transforms which attempt to decompose a signal into a set of functions of which

the linear combination is the original signal. Both EMD and AMD do not require the component functions to be related and attempt to have the modes have physical meaning rather than mathematical purity. EMD decomposes a signal by extracting the highest frequency signal into the first IMF. This occurs because the upper and lower envelopes ride on top of the high frequency signal and hug the underlying low frequency components allowing the high frequency signal to be stripped off. This behavior is inherent in EMD. In contrast, AMD requires that the current mode be the lowest frequency of the remaining modes so that the least square fit can ignore the remaining modes by allowing them to average out over cycles. Though EMD is more flexible because it can attack problems where the underlying physics may be completely unknown or unknowable, AMD was much more useful for the signal explored in this thesis.

6.2 Future Work

This thesis only touched the surface of this rich area of transform math. Improvements such as the adaptation of ℓ_1 optimization programs used in compressive sensing [19, 20] to this method look interesting. Possible further investigation may also lead to a deeper understanding of EMD itself. The validity of the AMD method was not tested against variation of all model parameters nor was it used to estimate all possible system parameters, so its ultimate limitations are not known. Most importantly, performance versus unmodeled dynamics was not considered, consideration of this would allow for an understanding of when AMD is appropriate. It was also considered,

but not implemented, that use of AMD to remove gross known effects and then apply EMD to the residual of unknown behavior may have a synergistic effect.

CHAPTER 7

BIBLIOGRAPHY

[1] S. M. Murrow, D.J., *Radar handbook, Second Edition, Chapter 20.* McGraw-Hill New York, 1990, vol. 1.

[2] S. M. Moore, R.K., *Radar handbook, Third Edition, Chapter 15.* McGraw-Hill New York, 2008, vol. 1.

[3] S. M. Wetzel, L.B., *Radar handbook, Third Edition, Chapter 16.* McGraw-Hill New York, 2008, vol. 1.

[4] W. George, *Introduction to Airborne Radar.* Hughes Aircraft, 1983.

[5] P. Swerling, "Probability of detection for fluctuating targets," *Information Theory, IRE Transactions on*, vol. 6, no. 2, pp. 269–308, 1960.

[6] M. Richards, *Fundamentals of radar signal processing.* McGraw-Hill, 2005.

[7] P. Beckmann and A. Spizzichino, *The scattering of electromagnetic waves from rough surfaces.* Artech House, Inc., 1987.

[8] J. Stratton, *Electromagnetic Theory*. McGraw Hill, 1941.

[9] A. Nashashibi, K. Sarabandi, S. Oveisgharan, M. Dobson, W. Walker, and E. Burke, "Millimeter-wave measurements of foliage attenuation and ground reflectivity of tree stands at nadir incidence," *Antennas and Propagation, IEEE Transactions on*, vol. 52, no. 5, pp. 1211–1222, 2004.

[10] Y. Wang, R. Zhang, and J. Sun, "On separating the information of slow-mode angular motion of projectile," in *Signal Processing (ICSP), 2010 IEEE 10th International Conference on*. IEEE, pp. 2125–2128.

[11] L. C. Ludeman, *Random Processes: Filtering, Estimation, and Detection*. Wiley, 2003.

[12] S. Orfanidis, *Introduction to signal processing*. Prentice-Hall, Inc., 2010.

[13] L. Cohen, *Time-frequency analysis*. Prentice-Hall, Inc., 1995.

[14] N. e. a. Huang, "The empirical mode decomposition and the Hilbert spectrum for nonlinear and non-stationary time series analysis," *Proceedings of the Royal Society A: Mathematical, Physical and Engineering Sciences*, vol. 454, no. 1971, pp. 903–995, 1998.

[15] S. A. Bhuiyan, "Fast and adaptive bidimensional empirical mode decomposition using order-statistics filter based envelope estimation and its applications for image processing," Ph.D. dissertation, 2009.

[16] J. F. Khan, "An emd based technique for pattern recognition," Ph.D. dissertation, Ph. D. dissertation, Dept. Elect. Eng., Univertisy of Alabama in Huntsville., Huntsville, AL, 2009.

[17] J. Proakis, *Digital communications*. McGraw-hill, 2001, vol. 1221.

[18] N. Huang, Z. Shen, and S. Long, "A NEW VIEW OF NONLINEAR WATER WAVES: The Hilbert Spectrum 1," *Annual Review of Fluid Mechanics*, vol. 31, no. 1, pp. 417–457, 1999.

[19] R. Baraniuk, "Compressive sensing [lecture notes]," *Signal Processing Magazine, IEEE*, vol. 24, no. 4, pp. 118–121, 2007.

[20] E. Candès, J. Romberg, and T. Tao, "Robust uncertainty principles: Exact signal reconstruction from highly incomplete frequency information," *Information Theory, IEEE Transactions on*, vol. 52, no. 2, pp. 489–509, 2006.